Mon. Not. R. Astron. Soc. **000**, 000–000 (0000) Printed 27 October 2015 (MN LATEX style file v2.2)

AGN Feedback, Host Halo Mass and Central Cooling Time: Implications for Galaxy Formation Efficiency and $M_{BH} - \sigma$

R. A. Main[1], B. R. McNamara[1,2,3], P. E. J. Nulsen[3,5], H. R. Russell[1,4], A. N. Vantyghem[1]
[1]Department of Physics and Astronomy, University of Waterloo, 200 University Avenue West, Waterloo, ON N2L 3G1, Canada
[2]Perimeter Institute for Theoretical Physics, 31 Caroline Street North, Waterloo, ON N2L 2Y5, Canada
[3]Harvard-Smithsonian Center for Astrophysics, 60 Garden Street, Cambridge, MA 02138, USA
[4]Institute of Astronomy, Madingley Road, Cambridge, CB3 0HA
[5]ICRAR, University of Western Australia, 35 Stirling Hwy, Crawley, WA 6009, Australia

arXiv:1510.07046v1 [astro-ph.GA] 23 Oct 2015

27 October 2015

ABSTRACT

We derive X-ray mass, luminosity, and temperature profiles for 45 galaxy clusters to explore relationships between halo mass, AGN feedback, and central cooling time. We find that radio–mechanical feedback power (referred to here as "AGN power") in central cluster galaxies correlates with halo mass, but only in halos with central atmospheric cooling times shorter than 1 Gyr. The 1 Gyr timescale corresponds approximately to the cooling time (entropy) threshold for the onset of cooling instabilities and star formation in central galaxies (Rafferty, McNamara & Nulsen 2008). No correlation is found in systems with central cooling times greater than 1 Gyr. The trend with halo mass is consistent with self-similar scaling relations assuming cooling is regulated by feedback. The trend is also consistent with galaxy and central black hole co-evolution along the $M_{\rm BH} - \sigma$ relation. AGN power further correlates with X-ray gas mass and the host galaxy's K-band luminosity. AGN power in clusters with central atmospheric cooling times longer than ~ 1 Gyr typically lies two orders of magnitude below those with shorter central cooling times. Galaxies centred in clusters with long central cooling times nevertheless experience ongoing and occasionally powerful AGN outbursts. We further investigate the impact of feedback on cluster scaling relations. We find $L-T$, and $M-T$ relations, excluding regions directly affected by AGN, that are consistent with the cluster population as a whole. While the gas mass rises, the stellar mass remains nearly constant with rising total mass, consistent with earlier studies. This trend is found regardless of central cooling time, implying tight regulation of star formation in central galaxies as their halos grew, and long-term balance between AGN heating and atmospheric cooling. Our scaling relations are presented in forms that can be incorporated easily into galaxy evolution models.

Key words: X-rays: galaxies: clusters — galaxies: cooling flows — galaxies: evolution — galaxies: active — galaxies: jets — accretion

1 INTRODUCTION

Energetic feedback from active galactic nuclei (AGN) has governed the growth of bulge galaxies from the quasar era (Silk & Rees 1997) through late times (Croton et al. 2006, reviewed by McNamara & Nulsen 2007, 2012; Fabian 2012). In the early Universe, quasar winds regulated the growth of galaxies by staving off accretion of molecular clouds, quenching both star formation and accretion onto the quasar itself (Silk & Rees 1998, reviewed by Alexander & Hickox 2012). As the Universe aged through redshift two to the present, the descendants of quasars – elliptical and brightest cluster galaxies (BCGs) – developed hot atmospheres of gas now observed in X-rays. Hot atmospheres serve as repositories of fuel from which elliptical galaxies and their supermassive black holes form. When an atmosphere's cooling timescale becomes shorter than the age of the system, the gas is expected to cool and accrete onto the galaxy fuelling both star formation and the AGN (Fabian 1994). A significant fraction of giant elliptical galaxies harbour radio AGN signalling on-

© 0000 RAS

going accretion onto massive black holes (Heckman & Best 2014). The binding energy they release in the form of radio jets and winds is captured by the hot atmospheres surrounding them (e.g., Churazov et al. 2000; McNamara et al. 2000; Bîrzan et al. 2004; Dunn, Fabian & Taylor 2005), creating buoyantly-rising bubbles and shock waves that heat the atmospheres suppressing cooling and regulating star formation (e.g., Nulsen et al. 2005; Forman et al. 2007; Blanton et al. 2011; Randall et al. 2011). In addition to heating, radio jets drive hot plasma (Simionescu et al. 2008; Kirkpatrick, McNamara & Cavagnolo 2011) and cold molecular outflows at rates of tens to hundreds of solar masses per year (Edge 2001; Salomé & Combes 2003; Russell et al. 2014; McNamara et al. 2014; Morganti et al. 2015). Flow rates of this magnitude rival or exceed the star formation rates in central galaxies (Kirkpatrick & McNamara 2015), thus they must be a significant aspect of the co-evolution of galaxies and massive black holes (Heckman & Best 2014). Much is not understood. For example, whether the outflowing gas leaves the galaxy entirely or returns to fuel future star formation and AGN activity is unclear (McNamara et al. 2014; Morganti et al. 2015). Nevertheless, radio-mechanical feedback is clearly an important (Croton et al. 2006; Bower et al. 2006) and long-term phenomenon that has persisted for at least the past 7 Gyr (Ma et al. 2011; Hlavacek-Larrondo et al. 2013; McDonald et al. 2013), or a substantial fraction of cluster ages.

The degree to which feedback affects cluster atmospheres as a whole is unclear. The most compelling, albeit indirect, evidence of AGN heating are departures of cluster scaling relations from simple power-law forms expected were clusters evolving under the influence of gravity alone (Kaiser 1986; Evrard & Henry 1991). For example, the observed $L-T$ and $L-M$ relations in clusters are steeper than the $L \propto T^2$, $L \propto M^{4/3}$ relations expected from self-similar evolution (see Giodini et al. 2013 for a review). Modeling has shown that the observed scaling relations can be reproduced when the energy released by AGN feedback and radiative cooling are included (Bialek, Evrard & Mohr 2001; Babul et al. 2002; Tozzi & Norman 2001; Voit et al. 2003; McCarthy et al. 2010; Short et al. 2010; Planelles et al. 2013). While the early "preheating" models of Kaiser, Evrard, and Henry conflict with observations of the Lyα forrest and the entropy profiles of cluster cores (reviewed by Kravtsov & Borgani 2012), recent observations indicate that continual heating by radio AGN, preferentially in lower mass clusters, may be able to supply the $\sim$ 1 keV per particle of heat needed to account for the observed scaling (Ma, McNamara & Nulsen 2013).

The declining fraction of baryons residing in stars above halo masses of $\sim 10^{12}$ $M_\odot$ (eg. David, Jones & Forman 1995; Behroozi, Wechsler & Conroy 2013; Gonzalez et al. 2013) may be another indication that AGN heating is significant on large scales. As halos become more massive, a progressively smaller fraction of the total mass is contained in stars despite the increasing fuel supply. At the same time, the total baryonic mass fraction (gas + stars) approaches the cosmic value with increasing halo mass. Interpreting the stellar mass fraction as a measure of the integrated star formation history, the declining ratio with mass implies mass-dependent quenching of star formation. It also indicates that the most massive halos are able to retain their baryons while less massive halos lose them (Balogh, Navarro & Morris 2000, Kravtsov, Vikhlinin & Meshscheryakov 2014). The prevalence of radio-mechanical feedback in giant elliptical galaxies(Best et al. 2007), and high power output in galaxy clusters (Vantyghem et al. 2014; Vikhlinin et al. 2006; McDonald et al. 2015) makes radio-mechanical AGN heating an appealing mechanism to prevent cooling and star formation, and perhaps an agent ejecting gas from lower mass halos.

In order to determine the degree to which radio-AGN are affecting the baryonic mass fraction and scaling relations, the relationship between halo mass and jet mechanical power must be explored. The measurement of cluster masses and scaling relations using a variety of techniques has been a burgeoning topic for decades, but primarily in the context of cosmology (Vikhlinin et al. 2006; Allen et al. 2006; Mahdavi et al. 2013; Mantz et al. 2010) and large scale structure formation (Clowe, Hoekstra, etc.). We address here the relationship between hydrostatic cluster masses and radio-mechanical feedback from supermassive black holes using a complete, flux-limited sample of clusters. We adopt standard methodologies using X-ray cavities and radio luminosities to estimate mechanical AGN jet power, and we focus here for the first time on relationships between jet power and halo mass. Using archival Chandra X-ray data and the Two Micron All-Sky Survey[1] (2MASS, Skrutskie et al. 2006), we investigate cluster scaling relations within our sample and compare them to previous measurements of the cluster population as a whole. We measure the scaling of gas mass with halo mass at R_{2500} and the relationship between stellar masses of BCGs and halo mass. We investigate how AGN power scales with several cluster properties, focussing on the critically important atmospheric cooling. We investigate the effect AGN feedback may have on on-going cluster scaling relations. We assume a cosmology with $\Omega_M = 0.3$, $\Omega_\Lambda = 0.7$, $H_0 = 70$ km s^{-1} Mpc^{-1}. All errors are quoted at the 1σ level.

2 SAMPLE AND DATA REDUCTION

2.1 Sample

We investigate the effects of radio-mode feedback in the HIghest FLUx Galaxy Cluster Sample (HIFLUGCS), a complete flux limited X-ray sample of 64 systems at galactic latitude $|b| > 20^o$ with X-ray flux $f_x > 2.0 \times 10^{-11}$ erg s^{-1} cm^{-2} in the 0.1-2.4 keV band (Reiprich & Böhringer 2002). All of the clusters in HIFLUGCS have been observed with Chandra, and 26 of these systems have observed X-ray cavities (Bîrzan et al. 2012). All 64 clusters in HIFLUGCS have detections or upper limits of 1.4 GHz radio emission of central radio sources. We use the 23 X-ray cavity systems with central cooling times below one Gyr to investigate the scaling relations of AGN mechanical power with cluster properties, since the AGN power in these systems is correlated with the cluster-scale properties of the ICM (Mittal et al. 2009, section 5). We refer to this subset throughout this paper as our primary sample. We use the 1.4 GHz emission to investigate AGN heating in the full HIFLUGCS sample in Section 5. Values used for the HIFLUGCS systems not in

[1] http://www.ipac.caltech.edu/2mass/

our primary sample are taken from the literature, and are referenced throughout.

We include an additional 27 clusters with radio cavities embedded in their X-ray atmospheres systems to extend the dynamic range of our sample. We refer to this as the extended sample throughout. This extended sample includes the systems in Rafferty et al. (2006) which are not in HIFLUGCS, and the clusters from the Massive Cluster Survey (MACS, Ebeling, Edge & Henry 2001) with clearly-defined cavities from Hlavacek-Larrondo et al. (2012). We additionally include the giant elliptical galaxies NGC5813 and NGC5846. Table 1 lists our sample and cleaned Chandra exposure times of all observations used.

2.2 Data Reduction

All observations were reprocessed with CIAO 4.6 using CALDB 4.5.9. Events were corrected for the time-dependent gain and charge transfer inefficiency and then filtered to remove those with bad grades. The improved background screening it enables was applied to all observations taken in VFAINT mode. Background light curves were extracted from the level 2 event files, and were filtered for flares using the LC_CLEAN[2] routine of M. Markevitch. Blank-sky backgrounds were extracted for each observation, processed identically to the event files, and reprojected to the sky position of the corresponding event files. The blank-sky backgrounds were normalized to match the 9.5-12.0 keV flux in the data set. All observations used, and final cleaned exposure times are detailed in Table 1.

3 ANALYSIS

3.1 X-ray Analysis

3.1.1 Spectral Extraction

Spectra were extracted from concentric circular annuli centred on the cluster centre. For systems with central surface brightness cusps, the centre was taken to be the position of the brightest pixel. For systems with no obvious central surface brightness peak, the cluster centre was taken to be the centroid of the X-ray emission. The inner regions of each cluster were excluded within the volume of the X-ray cavities. Point sources were detected using the WAVDETECT (Freeman et al. 2002) wavelet algorithm in CIAO, along with an image of the point spread function (PSF) to account for the degradation of the off-axis PSF. These point sources were confirmed by eye, and masked out in further analysis. Any known extended sources, or cluster substructure associated with mergers was also masked out of further analysis. The masked regions typically accounted for only a few percent of the total area.

Annuli enclose a minimum of ∼3000 counts permitting temperatures to be measured accurately in deprojection. Fewer source counts were required for low-temperature systems as emission lines make their temperature easier to determine. For systems with a very high number of source counts, we are limited by computational considerations rather than source counts. For these systems, the number of counts per annulus is chosen such that there are no more than ∼10-12 annuli per system. Spectra were extracted from these annuli in CIAO, and were grouped to have at least 30 counts per channel. Weighted redistribution matrix files (RMFs) were extracted using *mkacisrmf*, and weighted auxiliary response files (ARFs) were created using *mkwarf*. Spectra for observations on the same chip were summed together for observations of similar time period, and were kept separate otherwise. The ARFs and RMFs for the summed spectra were weighted according to the relative number of counts in each spectrum. The area lost to masked point sources, chip gaps, and so forth were accounted for.

To check for residual soft background emission, spectra were extracted from regions without any cluster emission. These spectra were then compared with the blank-sky backgrounds for consistency. In the case that the soft background was inconsistent with the blank-sky background, the residual emission was modelled by one or two soft thermal models with $Z/Z_{\odot} = 1$, $z = 0$ as described in Vikhlinin et al. (2005). The normalization was allowed to be negative to account for an over-subtraction of the soft backgrounds. In systems where the cluster emission is non-negligible over the entire detector, the additional soft background component is fit simultaneously with the cluster emission in the outermost annulus. The model for the soft background emission was scaled by the area of each annulus and added as a CORRFILE to each spectrum.

3.1.2 Mass Profiles: Hydrostatic Method

To calculate hydrostatic masses spectra were analysed in XSPEC using the NFWMASS mixing model (Nulsen, Powell & Vikhlinin 2010). This method assumes that the cluster is spherically symmetric, and that the X-ray emitting cluster gas is in hydrostatic equilibrium. The effects of non-thermal pressure at R_{2500} are expected to bias mass measurements low on the order of $10\% - 20\%$ (Nagai, Kravtsov & Vikhlinin 2007), but have also been found to be consistent with zero (Vikhlinin et al. 2009; Mahdavi et al. 2013). We use the additional assumption that the underlying gravitational potential follows the NFW profile (Navarro, Frenk & White 1997)

$$\rho(r) = \frac{\rho_0}{r/r_s(1 + r/r_s)^2}, \quad (1)$$

where ρ_0 is a characteristic density, and r_s is the scale radius. The NFW profile has been found to be an accurate description of cluster mass profiles, including systems with significant feedback (Pointecouteau, Arnaud & Pratt 2005; Vikhlinin et al. 2006; Schmidt & Allen 2007; Gitti et al. 2007). The full radial information of the temperature, gas density, and gravitating density are then given by r_s, $A = 4\pi G\rho_0 r_s^2 \mu m_H$, and a temperature for each annulus.

In conjunction with the NFWMASS model, each region was fit in the energy range $0.6 - 7.0$ keV by a PHABS(APEC) model in XSPEC version 12.8.0 (Arnaud 1996), using APEC version 2.0.2 (Foster et al. 2012). The spectra were fit using χ^2 minimization. The values of Anders & Grevesse (1989) were used for the solar abundances. The hydrogen column density (N_H) values were fixed to the galactic values of

[2] http://cxc.cfa.harvard.edu/contrib/maxim/acisbg/

Table 1. Target list and properties of our sample.

System	z	Exposure[a] (ks)	N_H[b] (10^{22}cm^{-2})	m_K	M_K	r_e[c] (kpc)	BCG Stellar Mass (10^{11} $M_\odot$)	M_{BH} (10^9 $M_\odot$)
2A0335+096	0.035	82.3	0.224	9.81±0.05	-26.18±0.05	44.3	5.07 ± 0.24	$1.2^{+2.7}_{-0.7}$
A85	0.055	37.4	0.039*	10.09±0.04	-26.72±0.04	50.8	6.92 ± 0.28	$2.0^{+4.2}_{-1.1}$
A133	0.057	109.4	0.0153	10.51±0.06	-26.35±0.06	28.9	6.34 ± 0.33	$1.4^{+3.1}_{-0.8}$
A262	0.016	108.6	0.089*	8.75±0.03	-25.66±0.03	28.9	2.61 ± 0.06	$0.8^{+1.7}_{-0.4}$
A478	0.088	135.2	0.281*	11.31±0.07	-26.68±0.07	67.8	8.07 ± 0.48	$1.9^{+4.1}_{-1.0}$
A496	0.033	52.4	0.04	9.81±0.02	-26.26±0.04	41.9	4.55 ± 0.17	$1.3^{+2.9}_{-0.7}$
A1795	0.063	391.5	0.041*	10.60±0.08	-26.47±0.08	69.7	5.32 ± 0.40	$1.6^{+3.4}_{-0.9}$
A2029	0.077	74.7	0.033	10.11±0.05	-27.42±0.05	72.2	13.2 ± 0.6	$3.6^{+7.7}_{-1.9}$
A2052	0.036	486.8	0.027	9.55±0.06	-26.33±0.06	51.2	4.85 ± 0.25	$1.4^{+3.0}_{-0.8}$
A2199	0.030	119.6	0.039*	9.17±0.03	-26.36±0.03	38.9	5.83 ± 0.18	$1.5^{+3.1}_{-0.8}$
A2204	0.152	69.7	0.061	12.24±0.19	-26.73±0.19	81.8	8.4 ± 1.4	$2.0^{+4.3}_{-1.1}$
A2597	0.085	108.5	0.0246	9.66±0.04	-25.63±0.04	40.6	3.08 ± 0.30	$0.8^{+1.7}_{-0.4}$
A4059	0.048	84.9	0.012	9.82±0.05	-26.67±0.05	58.4	8.03 ± 0.38	$1.9^{+4.1}_{-1.0}$
Centaurus	0.011	179.2	0.0854	7.14±0.02	-26.33±0.02	36.0	4.84 ± 0.11	$1.4^{+3.0}_{-0.8}$
Hydra A	0.055	152.6	0.0425	10.90±0.06	-25.91±0.06	33.8	3.43 ± 0.20	$1.0^{+2.1}_{-0.5}$
MKW3S	0.045	48.3	0.0286	10.85±0.06	-25.54±0.06	32.8	2.91 ± 0.16	$0.7^{+1.5}_{-0.4}$
NGC507	0.017	37.8	0.06	8.30±0.02	-25.94±0.02	28.4	3.92 ± 0.08	$1.0^{+2.2}_{-0.5}$
NGC1399	0.0048	145.2	0.0138	6.31±0.03	-25.26±0.03	22.0	2.21 ± 0.06	$0.6^{+1.2}_{-0.3}$
NGC1550	0.012	89.0	0.12*	8.77±0.03	-24.89±0.03	15.6	1.55 ± 0.04	$0.4^{+0.9}_{-0.2}$
NGC4636	0.0031	133.4	0.0185	6.42±0.04	-24.20±0.04	20.8	0.80 ± 0.03	$0.4^{+0.8}_{-0.2}$
NGC5044	0.0093	82.5	0.051	7.71±0.02	-25.31±0.02	16.3	2.25 ± 0.04	$0.6^{+1.2}_{-0.3}$
PKS1404-267	0.022	83.5	0.0431	9.57±0.03	-25.28±0.03	22.8	1.84 ± 0.06	$0.6^{+1.2}_{-0.3}$
Sersic159/03	0.058	90.3	0.039*	10.59±0.10	-26.33±0.10	73.4	4.82 ± 0.43	$1.4^{+3.0}_{-0.8}$
3C388	0.0917	32.2	0.0562	11.67±0.06	-26.24±0.06	41.0	-	$1.3^{+2.8}_{-0.7}$
3C401	0.201	30.8	0.0535	-	-	-	-	-
4C55.16	0.241	64.5	0.0449	13.84±0.13	-26.09±0.13	45.7	-	$1.2^{+2.5}_{-0.6}$
A1835	0.253	177.0	0.02	12.67±0.14	-27.37±0.14	70.8	-	$3.4^{+7.4}_{-1.8}$
Cygnus A	0.056	182.1	0.28*	10.28±0.06	-26.70±0.06	52.4	-	$1.9^{+4.1}_{-1.0}$
HCG62	0.0137	115.5	0.0355	8.63±0.03	-25.36±0.03	24.5	-	$0.6^{+1.3}_{-0.3}$
Hercules A	0.154	95.0	0.06	12.55±0.11	-24.46±0.09	56.1	-	$1.6^{+3.4}_{-0.8}$
MACSJ0159.8-0849	0.405	64.4	0.020	-	-	-	-	-
MACSJ0242.5-0253	0.314	8.0	0.029	-	-	-	-	-
MACSJ0429.6-0253	0.399	19.3	0.043	-	-	-	-	-
MACSJ0547.0-3904	0.319	19.2	0.037	-	-	-	-	-
MACSJ0913.7+4056	0.442	69.3	0.016	-	-	-	-	-
MACSJ1411.3+5212	0.464	74.1	0.0138	-	-	-	-	-
MACSJ1423.8+2404	0.543	105.5	0.022	-	-	-	-	-
MACSJ1532.8+3021	0.345	84.5	0.0248	-	-	-	-	-
MACSJ1720.2+3536	0.391	53.7	0.036	-	-	-	-	-
MACSJ1931.8-2634	0.352	91.0	0.08	-	-	-	-	-
MACSJ2046.0-3430	0.423	44.1	0.047	-	-	-	-	-
MACSJ2140.2-2339	0.313	33.2	0.036	-	-	-	-	-
MS0735.6+7421	0.216	447.2	0.031	13.32±0.17	-26.37±0.17	59.1	-	$1.5^{+3.1}_{-0.8}$
NGC5813	0.0065	-	-	7.41±0.03	-24.83±0.03	21.8	-	$0.4^{+0.8}_{-0.2}$
NGC5846	0.0057	-	-	6.94±0.02	-25.02±0.02	14.5	-	$0.5^{+1.0}_{-0.2}$
Perseus	0.018	449.5	0.133	8.13±0.04	-26.33±0.04	49.4	-	$1.4^{+3.0}_{-0.8}$
PKS0745-191	0.103	116.0	0.415	11.49±0.09	-26.82±0.09	52.0	-	$2.2^{+4.6}_{-1.1}$
RBS797	0.354	38.3	0.0256	-	-	-	-	-
Zw2701	0.215	95.8	0.007	13.42±0.17	-26.25±0.17	36.0	-	$1.3^{+2.8}_{-0.7}$
Zw3146	0.291	34.0	0.0224	13.88±0.28	-26.46±0.28	65.5	-	$1.6^{+3.4}_{-0.8}$

Notes: [a]Total cleaned exposure time. [b]N_H values marked with an asterisk are significantly different from the galactic value of Kalberla et al. (2005). [c]The extrapolation radius of the 2MASS K-band light profile.

Kalberla et al. (2005), except in systems where the best fit value was found to be significantly different. In these cases, we used the best fit N_H to spectra beyond the cool core. The N_H values used are listed in Table 1. Abundances were allowed to vary in the spectral fits, but were tied, as necessary, between adjacent annuli in the outer regions where the metallicity is nearly constant (De Grandi & Molendi 2001).

Galaxy cluster masses are typically measured to R_Δ, the radius within which the enclosed mass is Δ times the critical mass density at the cluster redshift. Then,

$$M_\Delta = \frac{4\pi R_\Delta^3}{3}\Delta\rho_c, \quad (2)$$

where $\rho_c = 3H^2/8\pi G$, $H = H_0E(z)$, and $E(z) = [\Omega_M(1+z)^3 + \Omega_\Lambda]^{1/2}$ in a flat Λ-CDM cosmology. We determine masses out to R_{2500}, as the Chandra data extend beyond it for the majority of our sample, and M_{2500} is then used as a proxy for cluster mass. The values of M_{2500} and R_{2500} are determined from the best fit NFW profile by numerically solving equation 2. In some nearby systems, extrapolation of the NFW profile was needed to reach R_{2500}. In these systems, the errors on M_{2500} are likely underestimated. All calculated values of M_{2500} are given in Table 2, and the systems where extrapolation to R_{2500} was needed are noted. The reduced χ^2 values of our spectral fits range between 0.89 and 1.32 with a mean value of 1.09. The Perseus cluster is an outlier with a reduced χ^2 value of 3.11. Perseus has exceptionally high quality data due both to being the brightest X-ray cluster in the sky and having deep exposures, and requires a multi-temperature model with multiple element abundances allowed to vary to accurately fit its spectra (e.g., Sanders et al. 2004). Our total mass profiles and gas mass profiles are presented in Appendix A.

As a calibration, we compare our mass measurements with other Chandra based hydrostatic measurements from the literature. We determine M_{2500} for the sample of clusters analyzed in Vikhlinin et al. (2006), except for Abell 2390 which was unconstrained. We also compare our M_{2500} values to those of Allen et al. (2008) and Sun (2009) in the systems that overlap our sample. We convert the mass measurements from the literature to a consistent cosmology, and compare our measurements in Figure 1. We find that our mass results are consistent within R_{2500} with no mass-dependent bias.

3.1.3 Mass Profiles: Remaining HIFLUGCS Systems

We derive M_{2500} for the remaining HIFLUGCS systems (i.e., HIFLUGCS systems not in our primary sample) using parameters in Reiprich & Böhringer (2002). *ROSAT*, *ASCA*, and *Einstein* observations were used to make these mass measurements, and likely have different systematics than our Chandra mass measurements. To correct for this, we compare how our mass measurements differ in the 24 systems where we have already determined M_{2500} using Chandra data. We find that the average ratio of our measurements to be $M_{2500}/M_{2500,\mathrm{Reiprich}} = 1.18$ with a standard deviation of 0.33. We apply this ratio to the M_{2500} values derived from Reiprich & Böhringer (2002) to estimate M_{2500} for the remainder of the HIFLUGCS systems. Measurements with this level of accuracy are sufficient for this study.

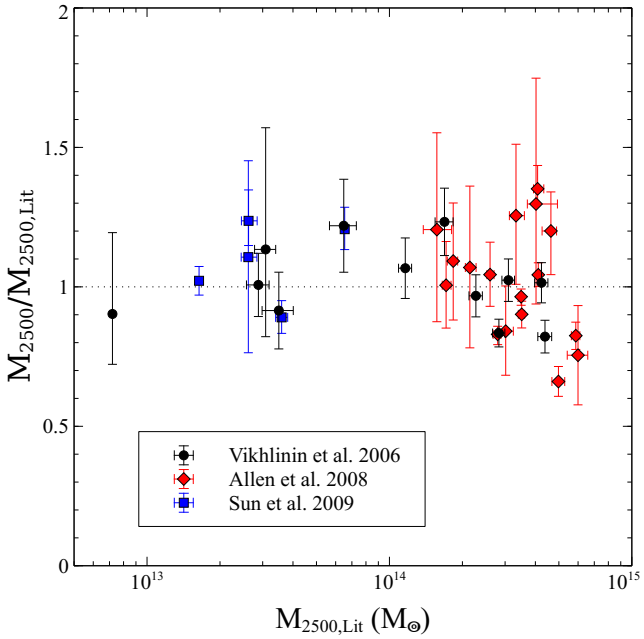

Figure 1. Comparison of a subsample of our masses to values in the literature.

3.1.4 Gas Mass

The gas density profiles were derived from the same set of spectra as our total masses, but with the central bin included. The spectra were fit in the $0.6-7.0$ keV range with using a PROJCT(PHABS*APEC) model in XSPEC, to obtain deprojected gas density profiles. The density profiles were then integrated in a piecewise manner from the centre of the cluster to obtain the radial gas mass distribution. From the gas mass profile, we derived M_g within R_{2500} (shown in Table 2). In systems where the data do not reach R_{2500}, M_g at R_{2500} was estimated by extrapolating an NFW profile fit to the inner profiles. The emissivity measurements of the outer bins may be artificially high as we assume no cluster emission beyond (see the gas mass profiles in Appendix A). Due to this effect, we have extrapolated our gas mass profiles for which only the final bin is beyond R_{2500}.

3.1.5 Luminosity and Temperature

We calculated the X-ray luminosity and temperature excluding the cluster cores. Spectra were extracted from apertures out to R_{2500} in each system, with the inner 0.3 R_{2500} excluded. These spectra were fit with a PHABS(APEC) model in XSPEC, along with an additional APEC model for the excess soft background when needed. The CFLUX model in XSPEC was used to calculate the unabsorbed flux in the energy range of 0.05 keV - 50 keV.

3.1.6 Central Cooling Time

Hudson et al. (2010) showed the central cooling time to be the best means of distinguishing a cool-core in systems with high quality X-ray data. When investigating the full HIFLUGCS sample, we separated the systems into two populations with central cooling times lying above and be-

low 1 Gyr. Central cooling time below 1 Gyr corresponds roughly to the cooling time threshold for the onset of star formation in central galaxies and is a strong indication of a cool-core (Rafferty, McNamara & Nulsen 2008; Cavagnolo et al. 2008; Mittal et al. 2009; Hudson et al. 2010). Cooling time profiles at the centres of clusters continue to decrease with radius (Panagoulia, Fabian & Sanders 2014), so it is important to define the central cooling time in a way that is unbiased by resolution. We use the t_c values of Hudson et al. (2010), where the central cooling times are all determined at a consistent radius of $0.004R_{500}$. This radius is resolved in all systems.

3.2 Cavity Energetics

The mechanical energy output from the central AGN can be directly measured from cavities observed in X-ray data (McNamara et al. 2000; Churazov et al. 2000; Bîrzan et al. 2004). Assuming the cavities are in pressure balance with the surrounding ICM, the minimum mechanical energy required to inflate the cavity is

$$E_{\rm cav} = \frac{\gamma}{\gamma - 1} pV, \tag{3}$$

where p is the pressure surrounding the cavity, V is the volume of the cavity, and γ is the adiabatic index of the medium filling the cavity. It is commonly assumed that the cavities are filled with relativistic plasma, as they are created by radio synchrotron emitting jets. In this case, $\gamma = 4/3$, and the energy output is $E_{\rm cav} = 4pV$. The mean power of the AGN is then estimated by dividing by the outburst age. AGN powers derived in this manner generally underestimate the total power (McNamara & Nulsen 2007). In this study, the buoyancy timescale of the cavities is used in all power calculations (McNamara et al. 2000; Churazov et al. 2000, 2001), which is calculated as

$$t_{\rm buoy} = R/v_t \simeq R\sqrt{SC/(2gV)}, \tag{4}$$

where S is the cross section of the bubble, and C is the drag coefficient taken as $C = 0.75$. The gravitational acceleration is calculated as $g \approx 2\sigma^2/R$, where σ is the stellar velocity dispersion. Cavity energies and power measurements are listed with references in Table 2.

3.2.1 Radio Luminosity

X-ray cavities are inflated by radio jets so we use the luminosity of central radio sources as a proxy for AGN activity. We have obtained monochromatic, 1.4 GHz radio luminosities of central radio sources for all of the HIFLUGCS objects from Mittal et al. (2009) and Bîrzan et al. (2012). In these studies, a radio source was deemed central if it is within $50h_{71}^{-1}$kpc of the X-ray peak. In systems without detected central radio sources, upper limits were estimated using the NVSS images by Bîrzan et al. (2012).

3.3 Stellar and Black Hole Mass

Apparent K-band luminosities taken from the 2MASS Extended Source Catalog are used to estimate stellar masses of the BCGs. Total masses were derived by extrapolating surface brightness profiles to the full radial extent of the galaxy. Stellar magnitudes were corrected for galactic extinction (Schlegel, Finkbeiner & Davis 1998), evolution, and K-corrections (Poggianti 1997). Absolute magnitudes were calculated assuming standard cosmological parameters, and redshifts in Table 1. Corrected B−V colours were taken from HyperLeda[3] (Paturel et al. 2003), and K-band luminosities were converted to stellar masses using the relation $\log(M/L_K) = -0.692 + 0.652(B - V)$ from Bell & de Jong (2001). For systems without B−V values in HyperLeda, we use the average B−V value of 0.86.

K-band luminosities (Graham 2007) were used to estimate the black hole masses as,

$$\log\left(\frac{M_{\rm BH}}{M_\odot}\right) = -0.37(\pm0.04)(M_K + 24) + 8.29(\pm0.08). \tag{5}$$

The scatter of 0.33 dex in this relation is included in the errors on our black hole masses.

Lauer et al. (2007) showed that the K-band magnitudes for BCGs from 2MASS do not capture the full extent of the stellar envelope and thus are likely to be underestimated. However, Batcheldor et al. (2007) find that black hole masses based on NIR magnitudes agree well with estimates based on the stellar velocity dispersion in BCGs. As such, the accuracy of our black hole estimates are unclear, and we take this into account in our interpretation of our results in section 4.4.

4 RESULTS AND DISCUSSION

4.1 Mass Partitioning

4.1.1 Gas Mass Fraction

In order to make contact with earlier studies, we first investigate the relationships between the total mass, gas mass, and stellar mass in our sample. We fit the relationship between the gas mass within R_{2500} and M_{2500} in HIFLUGCS systems using the bivariate correlated error and intrinsic scatter (BCES) method of Akritas & Bershady (1996). We find a tight correlation between halo mass and gas mass, shown in Figure 2, that follows the power law relationship $M_{g,2500}/10^{13}M_\odot = 10^{-1.27\pm0.05}(M_{2500}/10^{13}M_\odot)^{1.20\pm0.04}$. The slope of this relationship is consistent with Gonzalez et al. (2013).

This result implies that the gas fraction increases with halo mass. At the highest masses, the gas fraction is approximately 0.12, comparable to 0.11 found by Allen et al. (2008) in relaxed clusters with temperatures above 5 keV. These values lie below 0.155 derived from cosmic microwave background measurements (Ade et al. 2013), in part because we have not included stellar masses.

4.2 Cluster Scaling Relations

Before investigating the effects of AGN feedback on cluster scaling relations, we first investigate how the scaling relations in our sample compare to earlier work. If galaxy cluster formation was governed solely by gravity, the cluster luminosity, temperature, and mass should be related by simple

[3] http://leda.univ-lyon1.fr/

Table 2. System properties derived from Chandra X-ray Data.

System	P_{cav}[a] (10^{42} erg s^{-1})	pV (10^{58}erg)	M_{2500}[b] ($10^{13}M_\odot$)	Mg_{2500} ($10^{13}M_\odot$)	kT (keV)	L_{bol} (10^{42} erg s^{-1})	References
2A0335+096	24^{+23}_{-6}	$1.1^{+1.0}_{-0.3}$	10.4 ± 0.6	$1.04^{+0.03}_{-0.03}$	$3.46^{+0.09}_{-0.09}$	130^{+1}_{-1}	[1]
A85	37^{+37}_{-11}	$1.2^{+1.2}_{-0.4}$	20.6 ± 1.0	$2.40^{+0.06}_{-0.06}$	$6.6^{+0.1}_{-0.1}$	471^{+2}_{-2}	[1]
A133	620^{+260}_{-20}	24^{+11}_{-1}	12.4 ± 0.9	$1.04^{+0.06}_{-0.06}$	$4.4^{+0.1}_{-0.1}$	$96.1^{+0.8}_{-0.8}$	[1]
A262	$9.7^{+7.5}_{-2.6}$	$0.13^{+0.10}_{-0.03}$	3.2 ± 0.1	$0.283^{+0.009}_{-0.008}$	$2.23^{+0.04}_{-0.04}$	$27.8^{+0.2}_{-0.2}$	[1]
A478	100^{+80}_{-20}	$1.5^{+1.1}_{-0.4}$	43 ± 1.4	$5.4^{+0.3}_{-0.3}$	$7.5^{+0.3}_{-0.3}$	729^{+6}_{-6}	[1]
A496	172	2.34	13.3 ± 0.4	$1.17^{+0.08}_{-0.05}$	$4.5^{+0.1}_{-0.1}$	123^{+1}_{-1}	[2]
A1795	160^{+230}_{-50}	$4.7^{+6.6}_{-1.6}$	23.2 ± 0.3	$2.8^{+0.2}_{-0.2}$	$6.0^{+0.1}_{-0.1}$	366^{+3}_{-3}	[1]
A2029	87^{+49}_{-4}	$4.8^{+2.7}_{-0.1}$	33.8 ± 0.8	$3.6^{+0.1}_{-0.1}$	$8.0^{+0.1}_{-0.1}$	869^{+4}_{-4}	[1]
A2052	150^{+200}_{-70}	$1.7^{+2.3}_{-0.7}$	8.6 ± 0.1	$0.79^{+0.09}_{-0.09}$	$3.1^{+0.05}_{-0.05}$	90^{+1}_{-1}	[1]
A2199	270^{+270}_{-60}	$7.5^{+6.6}_{-1.5}$	17.4 ± 0.5	$1.65^{+0.01}_{-0.01}$	$3.9^{+0.2}_{-0.2}$	118^{+3}_{-3}	[1]
A2204	280^{+50000}_{-0}	5.6	55.2 ± 0.7	$6.0^{+0.2}_{-0.2}$	$9.2^{+0.3}_{-0.3}$	987^{+7}_{-7}	[3]
A2597	67^{+87}_{-29}	$3.6^{+4.6}_{-1.5}$	14.4 ± 0.2	$1.33^{+0.04}_{-0.04}$	$4.00^{+0.05}_{-0.05}$	175^{+1}_{-1}	[1]
A4059	96^{+89}_{-35}	$3.0^{+2.5}_{-0.9}$	15.3 ± 1.0	$1.02^{+0.04}_{-0.05}$	$4.4^{+0.2}_{-0.2}$	112^{+2}_{-2}	[1]
Centaurus	$7.4^{+5.8}_{-1.8}$	$0.060^{+0.051}_{-0.015}$	$^*8.2^{+0.2}_{-0.2}$	$0.056^{+0.007}_{-0.007}$	-	-	[1]
Hydra A	430^{+200}_{-50}	64^{+48}_{-11}	$16.0^{+1.2}_{-3.3}$	$1.65^{+0.03}_{-0.03}$	$3.79^{+0.07}_{-0.07}$	187^{+1}_{-1}	[1]
MKW3S	410^{+420}_{-44}	38^{+39}_{-4}	12.4 ± 1.3	$0.96^{+0.02}_{-0.02}$	$4.3^{+0.2}_{-0.1}$	$78.1^{+0.9}_{-0.9}$	[1]
NGC507	19^{+14}_{-7}	$0.35^{+0.06}_{-0.04}$	2.1 ± 0.3	$0.101^{+0.004}_{-0.004}$	$1.41^{+0.04}_{-0.04}$	$4.7^{+0.1}_{-0.1}$	[4],[5]
NGC1399	$1.2^{+0.5}_{-0.5}$	$0.11^{+0.05}_{-0.05}$	$^\dagger2.38^{+0.94}_{-0.90}$	-	-	-	[6]
NGC1550	15.4	0.17	1.67 ± 0.07	$0.11^{+0.01}_{-0.01}$	$1.27^{+0.03}_{-0.03}$	$5.5^{+0.2}_{-0.2}$	[2]
NGC4636	$2.76^{+0.56}_{-0.91}$	0.012	$^\dagger0.82^{+0.28}_{-0.28}$	-	-	-	[4],[5]
NGC5044	$4.2^{+1.2}_{-2.0}$	0.049	1.00 ± 0.05	$0.063^{+0.006}_{-0.005}$	$1.24^{+0.02}_{-0.02}$	$4.3^{+0.1}_{-0.1}$	[4],[5]
PKS1404-267	20^{+26}_{-9}	$0.12^{+0.15}_{-0.05}$	3.2 ± 0.1	$0.225^{+0.005}_{-0.005}$	$1.66^{+0.04}_{-0.05}$	$11.4^{+0.2}_{-0.2}$	[1]
Sersic159/03	780^{+820}_{-260}	25^{+26}_{-8}	9.5 ± 0.5	$0.84^{+0.03}_{-0.03}$	$2.53^{+0.04}_{-0.04}$	$71.9^{+0.4}_{-0.4}$	[1]
3C388	200^{+280}_{-80}	$5.2^{+7.5}_{-2.1}$	6.7 ± 0.9	$0.45^{+0.09}_{-0.09}$	$3.39^{+0.24}_{-0.16}$	44^{+1}_{-1}	[1]
3C401	650^{+1200}_{-420}	11^{+20}_{-7}	9.2 ± 2.7	$0.585^{+0.084}_{-0.066}$	$2.98^{+0.34}_{-0.31}$	49^{+2}_{-2}	[1]
4C55.16	420^{+440}_{-160}	12^{+12}_{-4}	21 ± 3	$1.93^{+0.08}_{-0.11}$	$5.0^{+0.2}_{-0.2}$	304^{+5}_{-5}	[1]
A1835	1800^{+1900}_{-600}	47^{+50}_{-16}	48 ± 2	$5.6^{+0.1}_{-0.1}$	$10.2^{+0.2}_{-0.2}$	1540^{+8}_{-8}	[1]
Cygnus A	1300^{+1100}_{-200}	84^{+70}_{-14}	17.3 ± 0.08	$1.73^{+0.06}_{-0.06}$	$7.61^{+0.21}_{-0.20}$	287^{+2}_{-2}	[1]
HCG62	$3.9^{+6.1}_{-2.3}$	$0.046^{+0.073}_{-0.028}$	1.70 ± 0.04	$1.0^{+2.7}_{-0.8}$	$1.06^{+0.02}_{-0.02}$	$1.97^{+0.05}_{-0.05}$	[1]
Hercules A	310^{+400}_{-90}	31^{+40}_{-9}	20.8 ± 1.4	$1.64^{+0.22}_{-0.18}$	$5.06^{+0.17}_{-0.17}$	179^{+2}_{-2}	[1]
MACSJ0159.8-0849	377	13.3	56 ± 6	$4.5^{+0.3}_{-0.3}$	$10.9^{+0.5}_{-0.6}$	1260^{+20}_{-20}	[7]
MACSJ0242.5-2132	353	8.96	23 ± 6	$2.4^{+0.2}_{-0.4}$	$6.5^{+1.0}_{-0.8}$	576^{+20}_{-20}	[7]
MACSJ0429.6-0253	83	2.17	20 ± 3	$2.22^{+0.38}_{-0.38}$	$8.1^{+1.5}_{-1.1}$	723^{+30}_{-30}	[7]
MACSJ0913.7+4056	7560	150	29 ± 4	$2.3^{+0.3}_{-0.3}$	$7.3^{+0.7}_{-0.6}$	523^{+20}_{-20}	[7]
MACSJ1411.3+5212	3560	49.1	17 ± 3	$1.83^{+0.17}_{-0.17}$	$6.0^{+0.5}_{-0.5}$	456^{+10}_{-10}	[7]
MACSJ1423.8+2404	1400^{+2500}_{-900}	61	27 ± 3	$2.6^{+0.2}_{-0.2}$	$8.2^{+0.8}_{-0.6}$	801^{+20}_{-20}	[7]
MACSJ1532.8+3021	2200^{+900}_{-900}	270	42 ± 8	$3.6^{+0.3}_{-0.3}$	$7.0^{+0.3}_{-0.3}$	867^{+10}_{-10}	[8]
MACSJ1720.2+3536	380	17.64	25 ± 5	$3.2^{+0.2}_{-0.2}$	$8.13^{+0.61}_{-0.56}$	899^{+20}_{-20}	[7]
MACSJ1931.8-2634	8760	83.4	52 ± 14	$4.4^{+0.3}_{-0.3}$	$7.9^{+0.4}_{-0.4}$	1060^{+10}_{-10}	[7]
MACSJ2046.0-3430	605	22.86	19 ± 5	$2.2^{+0.1}_{-0.2}$	$5.2^{+0.5}_{-0.4}$	451^{+10}_{-10}	[7]
MACSJ2140.2-2339	179	3.43	19 ± 2	$2.2^{+0.2}_{-0.2}$	$6.0^{+0.4}_{-0.4}$	479^{+10}_{-10}	[7]
MS0735.6+7421	6900^{+7600}_{-2600}	1600^{+1700}_{-600}	28.5 ± 0.9	$2.90^{+0.08}_{-0.08}$	$6.72^{+0.08}_{-0.08}$	523^{+2}_{-2}	[1]
NGC5813	$3.97^{+1.02}_{-2.36}$	0.064	$^\dagger0.088^{+0.004}_{-0.004}$	-	-	-	[4],[5]
NGC5846	$0.88^{+0.30}_{-0.59}$	0.0022	$^\dagger0.12^{+0.04}_{-0.04}$	-	-	-	[4],[5]
Perseus	150^{+100}_{-30}	19^{+20}_{-1}	$^*15.0^{+0.3}_{-0.3}$	$1.74^{+0.01}_{-0.01}$	-	-	[1]
PKS0745-191	1700^{+1400}_{-300}	69^{+56}_{-10}	33 ± 2	$4.0^{+0.2}_{-0.2}$	$8.0^{+0.2}_{-0.2}$	1200^{+10}_{-10}	[1]
RBS797	3340^{+1410}_{-1410}	38^{+50}_{-15}	50 ± 5	$3.8^{+0.4}_{-0.4}$	$9.1^{+0.7}_{-0.6}$	926^{+20}_{-20}	[1]
Zw2701	920^{+180}_{-180}	$42.0^{+0.8}_{-0.8}$	19 ± 1	$1.7^{+0.2}_{-0.2}$	$5.5^{+0.2}_{-0.2}$	267^{+4}_{-4}	[9]
Zw3146	5800^{+6800}_{-1500}	380^{+460}_{-110}	45 ± 10	$5.1^{+0.9}_{-1.2}$	$8.5^{+0.6}_{-0.4}$	1300^{+20}_{-20}	[1]

Notes: [a] pV and P_{cav} values taken from the references listed, using $E_{cav} = 4pV$. We assume factor of 2 errors in systems lacking quoted error bars. [b] Masses marked with a dagger are derived from Reiprich & Böhringer (2002), as described in section 5. References: [1] Rafferty et al. (2006), [2] Bîrzan et al. (2012), [3] Sanders, Fabian & Taylor (2009), [4] Cavagnolo et al. (2010), [5] Russell et al. (2013), [6] Shurkin et al. (2008), [7] Hlavacek-Larrondo et al. (2012), [8] Hlavacek-Larrondo et al. (2013), [9] Ma et al. in prep.

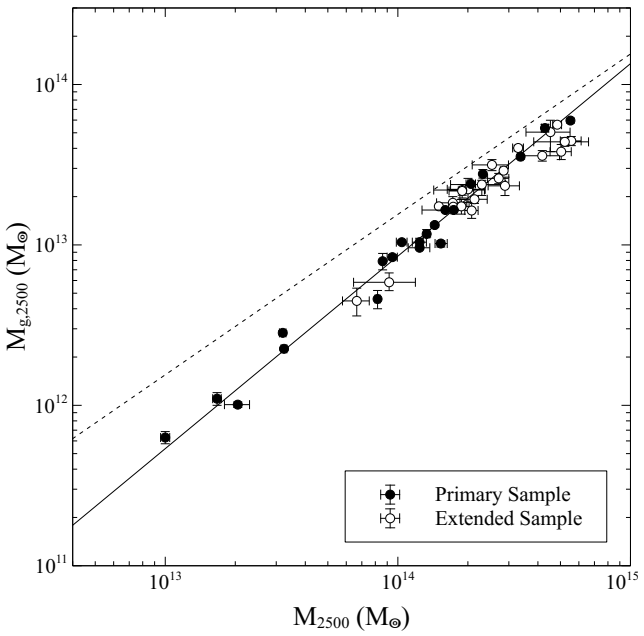

Figure 2. Gas mass within R_{2500} vs. M_{2500}. The solid line shows the best fit powerlaw to the primary sample, given by $M_{g,2500}/10^{13}M_\odot = 10^{-1.27}(M_{2500}/10^{13}M_\odot)^{1.2}$. The dotted line shows the Planck value of $\Omega_b/\Omega_m = 0.155$ (Ade et al. 2013)

powerlaw expressions, as $L \propto E(z)T^2, M \propto E(z)^{-1}T^{3/2}$, where $E(z) = H(z)/H_0$ (Kaiser 1986). Departures from these relations are likely caused by baryonic processes, such as radiative cooling and heating by AGN and supernovae (reviewed by Kravtsov & Borgani 2012). Here we search for indications that these scaling relations are affected by ongoing AGN feedback.

We fit the $L-T$ and $M-T$ relations with the bivariate correlated error and intrinsic scatter (BCES) method of Akritas & Bershady (1996). Previous studies have found deviations from self-similarity are largest in poor clusters and groups (Arnaud, Pointecouteau & Pratt 2005; Sun 2009; Eckmiller, Hudson & Reiprich 2011). We perform fits on both our entire sample and only the systems with temperatures above 3 keV. We also fit our sample omitting evolutionary corrections to allow a direct comparison to the results in section 4.3.

4.2.1 L-T relation

The luminosities calculated for a flux limited sample are affected by the Malmquist bias, which over-represents the most luminous objects. For a low-redshift sample with a log-normal distribution of luminosities and no redshift cutoff, the bias on L in the $L-T$ relation can be expressed as $\Delta \ln L = \frac{3}{2}\sigma^2$, where σ is the log normal scatter in L for a given temperature (described in Vikhlinin et al. 2009 for the $L-M$ relation). This will be equivalent for any relation between L and a second variable, if they are related by a powerlaw with log-normal scatter. Correcting for the Malmquist bias in our sample then simply modifies the normalization of our relations involving luminosity.

The best fit results to our $L-T$ and $M-T$ relations are given in table 3, and are shown in figure 3. Our fit to the full sample is $L_{\rm bol}E(z)^{-1} \propto T^{2.63\pm0.10}$. This slope is significantly steeper than the self-similar value, but is consistent with the range of slopes of core-excised $L-T$ relations found in previous studies (see Giodini et al. 2013 for a review). This includes $L-T$ relations measured for the full cluster population and in non cool-core clusters (Markevitch 1998; Zhang et al. 2008; Eckmiller, Hudson & Reiprich 2011; Maughan et al. 2012). Additionally, the best fit slope in our systems above 3 keV is not found to be significantly different from the result for the full sample. Our normalization is lower than previous studies due to aperture size.

4.2.2 M-T relation

The best fit $M-T$ relation is given by $(M_{2500}/10^{13}M_\odot)E(z) = 10^{0.02\pm0.07}T^{1.87\pm0.12}$ keV for our full sample, and $(M_{2500}/10^{13}M_\odot)E(z) = 10^{0.14\pm0.14}T^{1.68\pm0.22}$ keV when fit to systems with $T > 3$ keV. The $M-T$ relation is steeper than the self-similar expectation for our full sample, and is consistent with $M \propto T^{3/2}$ when only the $T > 3$ keV systems are fit. The normalization of our relation is slightly higher than those of Arnaud, Pointecouteau & Pratt (2005) and Vikhlinin et al. (2006), but this difference is insignificant. A slope of 1.87 ± 0.12 is marginally steeper than the slopes of $\sim 1.6-1.7$ which is usually observed over the same mass range (e.g.,Arnaud, Pointecouteau & Pratt 2005; Vikhlinin et al. 2006). Due to the small number of points at low mass, this could easily be caused by one or two outliers. For example, excluding NGC 5044, the best fit slope is 1.77 ± 0.10. We find no convincing evidence that the $M-T$ relation in our sample is significantly different from previously measured relations.

4.2.3 Summary of scaling relations results

We measured the $L-T$ and $M-T$ relations in our sample of clusters experiencing AGN feedback, excluding the inner 0.3 R_{2500}. Both relations are steeper than the self-similar slopes. The $M-T$ relation is consistent with the self-similar scaling, but only in clusters with mean temperatures above 3 keV. Our scaling relations are consistent with previous studies which included the full cluster population, and studies of non cool-core clusters. The scaling for regions beyond the cooling cores are consistent with the cluster population as a whole. This result seems to imply either that mechanical AGN feedback is not strongly affecting the overall temperature and luminosity of clusters beyond the cooling radius (Mantz et al. 2010), or that all clusters have experienced a significant level of heating from AGN or other processes in the past.

4.3 Relationship between Jet Power and Dark Matter Halo Mass

Using scaling arguments (Kaiser 1986), we now consider how the jet powers of AGN at the centers of cluster cool cores are expected to scale with the properties of their hosts. In the spirit of scaling models, we ignore all but the most basic physical processes. Hence, we assume that the jet mechanical power is the dominant heat source that prevents the hot

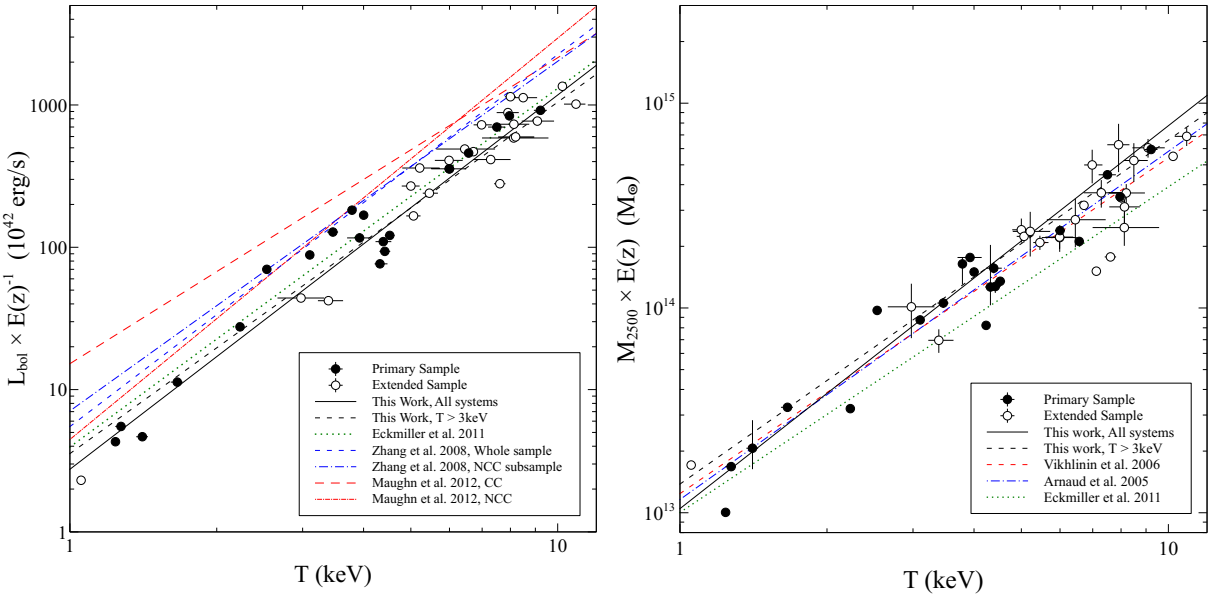

Figure 3. *Left:* Bolometric luminosity vs temperature. *Right:* M_{2500} vs. temperature. Luminosity and temperature are measure in the aperture (0.3-1.0)R_{2500}. The black lines show the best fit relation to the primary sample over the full range, and restricted to systems with T > 3 keV. Best fit relations from the literature for core-excised L-T relations, and the M-T relation within R_{2500} are overlain. The discrepancy between the L-T normalizations is primarily due to differences in the aperture used to determine the luminosity.

Table 3. Cluster Scaling Relations.

Fit Results to log(y) $= a + b$ log(x)

y	x	a	b	σ
$L_{\rm bol}E(z)^{-1}$	T_x	0.44(±0.07)	2.63(±0.10)	0.15
$L_{\rm bol}E(z)^{-1}$	$T_x(>3$keV)	0.55(±0.26)	2.47(±0.34)	0.15
$M_{2500}E(z)$	T_x	0.02(±0.07)	1.87(±0.12)	0.11
$M_{2500}E(z)$	$T_x(>3$keV)	0.14(±0.14)	1.68(±0.22)	0.08
$L_{\rm bol}$	T_x	0.43(±0.07)	2.76(±0.09)	0.15
$L_{\rm bol}$	M_{2500}	0.40(±0.11)	1.55(±0.09)	0.15
M_{2500}	T_x	0.02(±0.07)	1.78(±0.11)	0.11
$M_{g,2500}$	M_{2500}	−1.27(±0.05)	1.20(±0.04)	0.07

Notes: σ is the RMS residual, $L_{\rm bol}$ is the core-excised luminosity in units of 10^{42} erg s^{-1}, T_x is the core-excised temperature in keV, and M_{2500} and $M_{g,2500}$ are in units of $10^{13}M_\odot$.

gas from cooling in every cluster cool core. Thus, for the central AGN to regulate cooling and star formation by feedback, its mean jet power must, at least, match the power radiated by the gas that could otherwise cool to low temperatures, i.e. the cooling power. The cooling power, $L_{\rm cool}$, is estimated as the power radiated by gas within the cooling radius, $R_{\rm cool}$, where the gas cooling time equals the age of the cluster. Although feedback has a significant impact on the gas distribution within $R_{\rm cool}$, gas outside this radius is much less affected (because the total thermal energy of the gas is a strongly increasing function of the radius in the region of interest in most clusters). Voit, Kay & Bryan (2005) argues that the entropy index, $\Sigma = kT/n_{\rm e}^{2/3}$, varies with radius as $\Sigma \propto R^\eta$, with $\eta \simeq 1.1$, in the self-similar regions of clusters, $R > R_{\rm cool}$. Treating cluster atmospheres as isothermal, this implies that the electron density scales as

$$n_{\rm e} \sim f_{\rm g}\overline{\rho}(R/R_{\rm v})^{-3\eta/2}, \tag{6}$$

where $R_{\rm v}$ is the virial radius, $\overline{\rho}$ is the mean mass density of the cluster within the virial radius and $f_{\rm g}$ is the gas fraction. The cooling time scales as $T/(n_{\rm e}\Lambda)$, where we assume that the cooling function, Λ, scales with temperature as $\Lambda(T) \propto T^\alpha$. Equating the cooling time to the cluster age, $t_{\rm age}$, then gives the scaling for $R_{\rm cool}$,

$$\left(\frac{R_{\rm cool}}{R_{\rm v}}\right)^{3\eta/2} \sim \frac{f_{\rm g}\overline{\rho}t_{\rm age}}{T^{1-\alpha}}. \tag{7}$$

Observed entropy and gas density profiles are less steep in the core region affected by AGN feedback than in the self-similar region beyond $R_{\rm cool}$, so that the cooling luminosity is dominated by radiation from around $R_{\rm cool}$. For gas pressure p, this justifies the scaling approximation for the cooling power

$$\begin{aligned} L_{\rm cool} &\sim \frac{p(R_{\rm cool})R_{\rm cool}^3}{t_{\rm age}} \sim \frac{f_{\rm g}MT}{t_{\rm age}}\left(\frac{R_{\rm cool}}{R_{\rm v}}\right)^{3-3\eta/2} \\ &\sim f_{\rm g}^{2/\eta}MT^{\{1-[(2/\eta)-1](1-\alpha)\}}\overline{\rho}^{[(2/\eta)-1]}t_{\rm age}^{(2/\eta)-2}. \end{aligned} \tag{8}$$

Here, the second scaling uses $p \sim n_{\rm e}T$, with the scaling relation (6) and the mass scaling $\overline{\rho}R_{\rm v}^3 \sim M$. The final expression is obtained by using the relation (7) to eliminate $R_{\rm cool}/R_{\rm v}$. Under the usual self-similar scaling assumptions, cooling is dominated by thermal bremsstrahlung, so $lpha = 0.5$ and $T \sim M^{2/3}\overline{\rho}^{1/3}$, so that the mass dependence of the cooling power is contained in $L_{\rm cool} \sim f_{\rm g}^{2/\eta}M^{2-[2/(3\eta)]} \sim f_{\rm g}^{1.82}M^{1.39}$ for $\eta = 1.1$, or $P_{\rm cav} \sim M^{1.75}$ using $f_{\rm g} \sim M^{0.2}$ measured in section 4.1.1. Strictly, the self-similar model has constant $f_{\rm g}$, so that its inclusion here highlights a weakness of the model. Nevertheless, observed gas fractions increase with cluster mass and we should expect this to steepen the mass dependence of feedback power.

Table 4. Mass Dependence of Feedback

Fit Results to $\log(y) = a + b\,\log(\mathrm{x})$

x	y	a	b	σ^a
Primary				
$M_{2500}{}^b$	$P_{\rm cav}{}^c$	0.32(±0.24)	1.55(±0.26)	0.56(±0.08)
M_{2500}	$E_{\rm cav}{}^d$	−1.13(±0.25)	2.04(±0.30)	0.70(±0.09)
M_{2500}	$L_{1.4\rm GHz}{}^e$	−3.52(±0.24)	2.51(±0.33)	0.89(±0.14)
$M_{\rm K}{}^f$	$P_{\rm cav}$	−27.7(±5.3)	−1.13(±0.20)	0.72(±0.09)
$M_{\rm K}$	$E_{\rm cav}$	−36.4(±7.0)	−1.43(±0.27)	0.93(±0.15)
$M_{\rm K}$	$L_{1.4\rm GHz}$	−48.5(±7.1)	−1.83(±0.28)	1.11(±0.20)
Extended				
M_{2500}	$P_{\rm cav}$	0.04(±0.20)	2.03(±0.17)	0.60(±0.06)
M_{2500}	$E_{\rm cav}$	−1.43(±0.25)	2.51(±0.22)	0.73(±0.08)
$M_{\rm K}$	$P_{\rm cav}$	−36.0(±4.6)	−1.46(±0.18)	0.78(±0.09)
$M_{\rm K}$	$E_{\rm cav}$	−48.6(±6.3)	−1.90(±0.24)	1.06(±0.13)

Notes: $^a\sigma$ is the RMS residual. $^bM_{2500}$ is in units of $10^{13}M_\odot$. $^cP_{\rm cav}$ is given in units of 10^{42} erg s^{-1}. $^dE_{\rm cav}$ is in units of 10^{58}erg. $^eL_{1.4\rm GHz}$ is given in units of 10^{40}Hz. ^{f}The K-band luminosity of the BCG from 2MASS.

Sijacki & Springel (2006) proposed an alternative scaling model, based instead on the properties of the supermassive black in the central AGN. Their key assumptions are, first, that the jet power is a small, fixed fraction of the Eddington luminosity, so that the jet power is proportional to the mass of the black hole, $M_{\rm BH}$. Secondly, using the observed relationship, $M_{\rm BH} \sim \sigma^4$ (Gebhardt et al. 2000; Tremaine et al. 2002), and assuming that the relevant velocity dispersion scales like that of the whole cluster gives $M_{\rm BH} \sim T^2 \sim M^{4/3}$. Using the alternative scale, $M_{\rm BH} \sim \sigma^5$ (Ferrarese & Merritt 2000), the same argument would give $M_{\rm BH} \sim M^{5/3}$.

Whether SMBH co-evolution is tied more closely to the bulge or the dark matter halo itself is not understood (Ferrarese 2002; Kormendy & Ho 2013). Bluck et al. (2014) find that quenching in central galaxies is most tightly coupled to the bulge mass, and suggest AGN feedback as the most likely quenching mechanism. In order to examine this question, we compare AGN energetics with M_{2500} and with M_K of the BCG.

We fit power law relationships between $E_{\rm cav}$, $P_{\rm cav}$, and $L_{1.4\rm GHz}$. A2204 is excluded from our fits due to the large systematic uncertainty in the energetics of the outer cavity system (Sanders, Fabian & Taylor 2009). The error on the scatter is calculated through bootstrap resampling with 10000 iterations. The relations for $\rm M_{2500}$ and $\rm M_K$ are plotted in Figure 4, and are listed in Table 4 with the 1-σ logarithmic vertical scatter.

In the primary sample, we find best fitting relation between cavity energy and halo mass, $E_{\rm cav} \propto M_{2500}^{2.04\pm0.30}$. The best fitting relationship between jet power and halo mass, $P_{\rm cav} \propto M_{2500}^{1.55\pm0.26}$, is consistent with our self-similar model scaling of (8), and with the Somerville et al. (2008) semi-analytic model that assumes jet power scaling with black hole mass as $M_{\rm BH}^1$.6. The relation between $P_{\rm cav}$ and M_{2500} is further consistent with the model detailed in Sijacki & Springel (2006) with $P_{\rm cav} \propto M_{\rm BH}$ and an M-σ relation of $M_{\rm BH} \propto \sigma^4$ or $M_{\rm BH} \propto \sigma^5$. The relation between $E_{\rm cav}$ and M_{2500} is steeper than either of these models, but favours co-evolution of the forms $P_{\rm cav} \propto M_{\rm BH}$, and $M_{\rm BH} \propto \sigma^5$. The assumption that $E_{\rm cav} \propto M_{\rm BH}$ is equivalent to fixing accretion to be proportional to the Eddington rate (e.g., Somerville et al. 2008, which we investigate further in Section 4.4.

The extended sample yields steeper scalings of the forms $P_{\rm cav} \propto M_{2500}^{2.03\pm0.17}$ and $E_{\rm cav} \propto M_{2500}^{2.51\pm0.22}$, both of which are steeper than the primary sample and the simple analytic model of (Sijacki & Springel 2006). As the extended sample includes higher redshift clusters, its steepening could be either a real evolutionary effect or selection bias introduced by our insensitivity to low power AGN at higher redshifts that would lie below the relation. We cannot distinguish between these possibilities. Nevertheless, having been drawn from a complete, flux-limited sample, the results for the primary sample are reliable.

4.3.1 Scaling between AGN Power, Gas, and Stellar Mass

The dependence of $P_{\rm cav}$ on gas mass is similar to that on total mass. The RMS residual of $P_{\rm cav}$ on gas mass is 0.54±0.08, and the fits are equally good for gas and total mass. The situation is much the same for T, $L_{\rm bol,total}$, $L_{\rm bol,exc}$, due to the close relationship between the gas and total masses. Assuming the black hole is fuelled by gas, jet power would more naturally be expected to correlate with gas mass. However, we find no evidence that gas mass is preferred over total mass.

The scatter in the trend between jet power and the BCG's K-band magnitude (a proxy for stellar mass) in Figure 4 is larger than that for the trend with M_{2500} for both the primary and extended samples. This indicates that stellar mass is not the primary factor determining jet power. As a check we used the 1.4 GHz luminosity as an independent proxy for mechanical power. We find that the scatter in the relationship between $L_{1.4\rm GHz}$ and M_{2500} is 0.89 ± 0.14 dex and the scatter for M_K is 1.11 ± 0.20 dex. The difference is insignificant.

4.3.2 Correlation Bias

A biased cavity detection procedure could potentially affect the scaling relations involving cavity power. One possible source of bias would be a preferred angular size for detectable cavities due to Chandra's spatial resolution. The most obvious manifestation would be a spurious correlation with redshift. Cavity power would scale as D_A^2, since $V \propto D_A^3$, and $t_{\rm buoy} \propto D_A$. In a flux-limited sample, this would cause a spurious correlation between cavity power and X-ray luminosity.

The angular areas of the cavities in our systems are plotted against angular diameter distance in Figure 5. The areas span 3 decades and, on average, decrease with redshift. This trend is inconsistent with a preferred angular size, and implies no spurious redshift dependence. Thus our correlations of cavity power with redshift dependent quantities are likely physical trends.

Several other factors suggest a genuine relationship between halo mass and $P_{\rm cav}$. It is unlikely that much more powerful outbursts are missed in the nearby, low-mass systems as

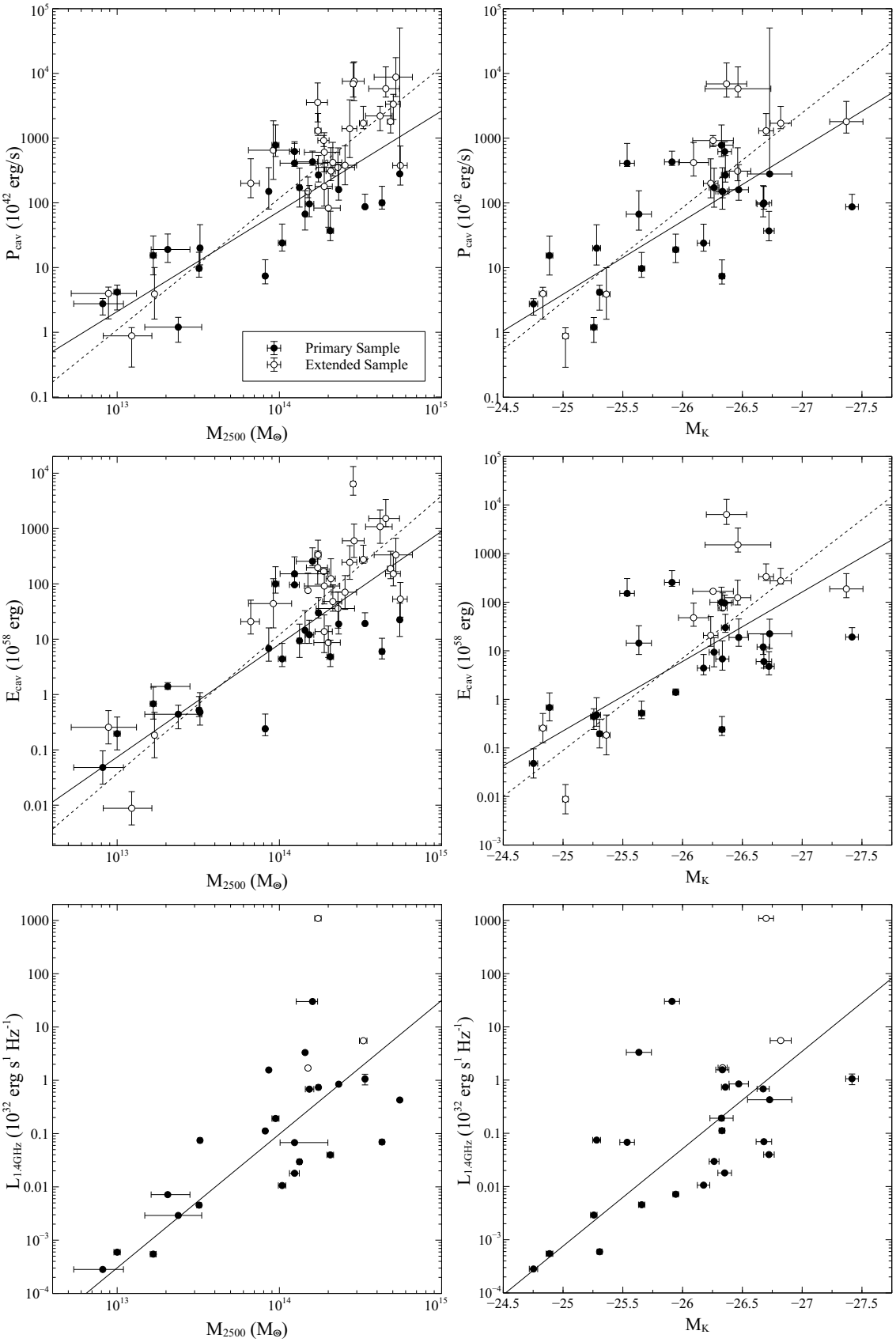

Figure 4. Top: Cavity power vs. M_{2500} (*Left*) and vs. M_K (*Right*). Middle: Cavity energy vs. M_{2500} (*Left*) and vs. M_K (*Right*). Bottom: 1.4GHz luminosity vs. M_{2500} (*Left*) and vs. M_K (*Right*). The solid and dashed lines denotes the best BCES bisector fit for the primary and extended samples respectively. Cavity energy calculated as $E_{cav} = 4pV$, and the buoyancy timescale is used in calculating P_{cav}.

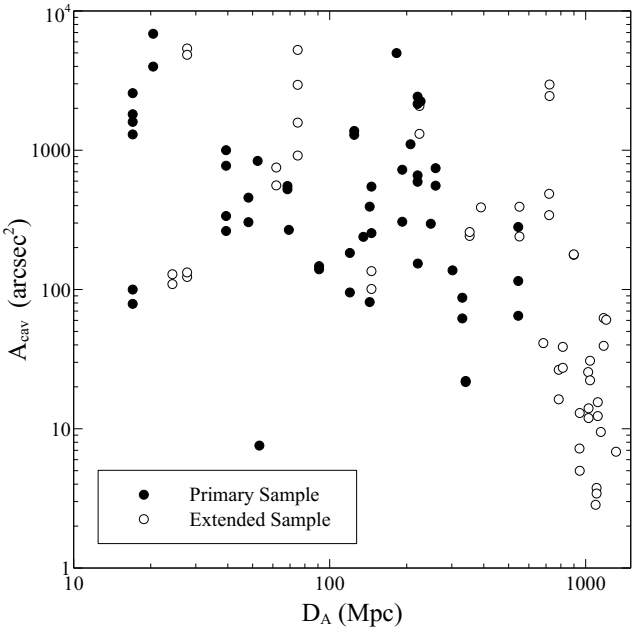

Figure 5. Angular area of all detected cavities in our sample vs. angular diameter distance. If there is a bias towards detecting a specific angular size of cavities, the relation should appear flat with small scatter.

they would be easily detected. In the full HIFLUGCS sample, we also find a strong correlation in clusters with short central cooling times between jet power and halo mass when using 1.4 GHz luminosity as a proxy for jet power (see Figure 9 and Section 5.1). All HIFLUCGS clusters with central cooling times below 1 Gyr are radio loud. Therefore, we are missing few if any objects to the bottom-right or top-left of the relationship between $P_{\rm cav}$ and M_{2500}. Therefore, the correlation is likely real.

4.3.3 Integrated star formation efficiency

We now investigate the potential impact of AGN feedback on the efficiency of star formation, adopting the ratio of the BCG's stellar mass to the total baryon mass as a probe. We do not consider the masses of satellite galaxies in the core (e.g., Kravtsov, Vikhlinin & Meshscheryakov 2014), but note that the BCG dominates the stellar mass there (Burke, Hilton & Collins 2015).

We plot the fraction of baryons in stars against both gas mass and stellar mass in Figure 6. These diagrams show that that the gas fraction locked-up in stars declines with total gas mass from a value of about 20% in groups with baryon masses of $\sim 10^{12}$ M$_\odot$ to roughly 1% or less in the centres of rich clusters with gas masses upward of 10^{14} M$_\odot$. Interpreted as the efficiency of conversion of gas into stars, the integrated star formation efficiency of BCGs decreases dramatically with the total gas and halo masses, as previously observed (e.g. David, Jones & Forman 1995; Behroozi, Wechsler & Conroy 2013; Gonzalez et al. 2013). The trend is sharper when restricting the measurement to stellar mass within a 20 kpc aperture, indicating that the central stellar mass is remarkably consistent from galaxy to galaxy.

The right hand panels of Figure 6 show that the more massive halos harbour somewhat more massive BCGs. However, the stellar mass range is much smaller than the range of halo mass and increases with halo mass with an amplitude no larger than the scatter in the trend. The data show that BCGs have grown to a relatively narrow range of masses despite the enormous fuel supply available to continue fuelling their growth. BCGs residing in low mass halos containing almost 30% of the baryonic mass within R_{2500}, consumed their fuel supplies more efficiently than BCGs in the highest mass systems, which consumed only $1-2$% of the baryonic mass within R_{2500}.

4.3.4 Effects of Cooling Atmospheres

In order to convert the fuel reserves locked-up in hot atmospheres into stars, the gas must cool and accrete into the centre of the halo. In order to investigate the potential effects of cooling atmospheres on the integrated star formation efficiency in BCGs, we compare the stellar mass to the halo mass in the HIFLUGCS sample. We examine the relationship between the ratio of stellar to halo mass $M_{*,\rm BCG}/M_{2500}$ and halo mass M_{2500} in clusters with and without cooling atmospheres. To isolate the cooling and non-cooling atmospheres, we have divided the sample by central cooling time, indicating those clusters whose central cooling times above and below 1 Gyr, which corresponds approximately to the cooling time threshold above which cold clouds and star formation are observed in BCGs (Rafferty, McNamara & Nulsen 2008).

We find no discernible separation between BCGs with long and short central cooling times in the left panel of Figure 7. Although most BCGs with short central cooling time are forming stars, recent star formation has apparently contributed little to the total stellar mass of the galaxies. If cooling and star formation were able to ensue unimpeded over the past several Gyr, the gas available within the cooling radius should fuel enough star formation to significantly increase the stellar mass.

In order to examine this question quantitatively, we calculated the gas mass within the cooling region and added it to the observed stellar mass to estimate how much the galaxies would have grown had this gas formed stars. The values of $r_{\rm cool}$ represent the radius within which the cooling time of the ICM is less than 7.7 Gyr, taken from Bîrzan et al. (2012). In those systems where we do not have the full gas mass profile, the gas mass within $r_{\rm cool}$ was estimated assuming the gas density follows an NFW profile with $c_{500} = 3$, a typical value for halos in our mass range (Vikhlinin et al. 2006), and $M_{g,2500}$ is calculated using $M_g/10^{13}M_\odot = 10^{-1.27}(M_{2500}/10^{13}M_\odot)^{1.20}$ derived in section 4.1.1. The value $(M_{*,\rm BCG}+M_g(<r_{\rm cool}))/M_{2500}$ then indicates how much the BCG would have grown if the hot atmosphere had cooled efficiently and formed stars shown in the right panel of Figure 7. A comparison between the left panel of Figure 7, showing BCGs as they are, and the right panel which shows their mass had the cooling gas formed stars, indicates the dramatic difference in their masses by factors of several to nearly a factor of 10. That BCGs do not segregate in this diagram is a graphic indication of how efficiently cooling has been suppressed. Virial shocks in groups and clusters heat accreting gas, which limits the cooling gas that can reach the BCG in halos above $\sim 10^{12}M_\odot$ (Dekel

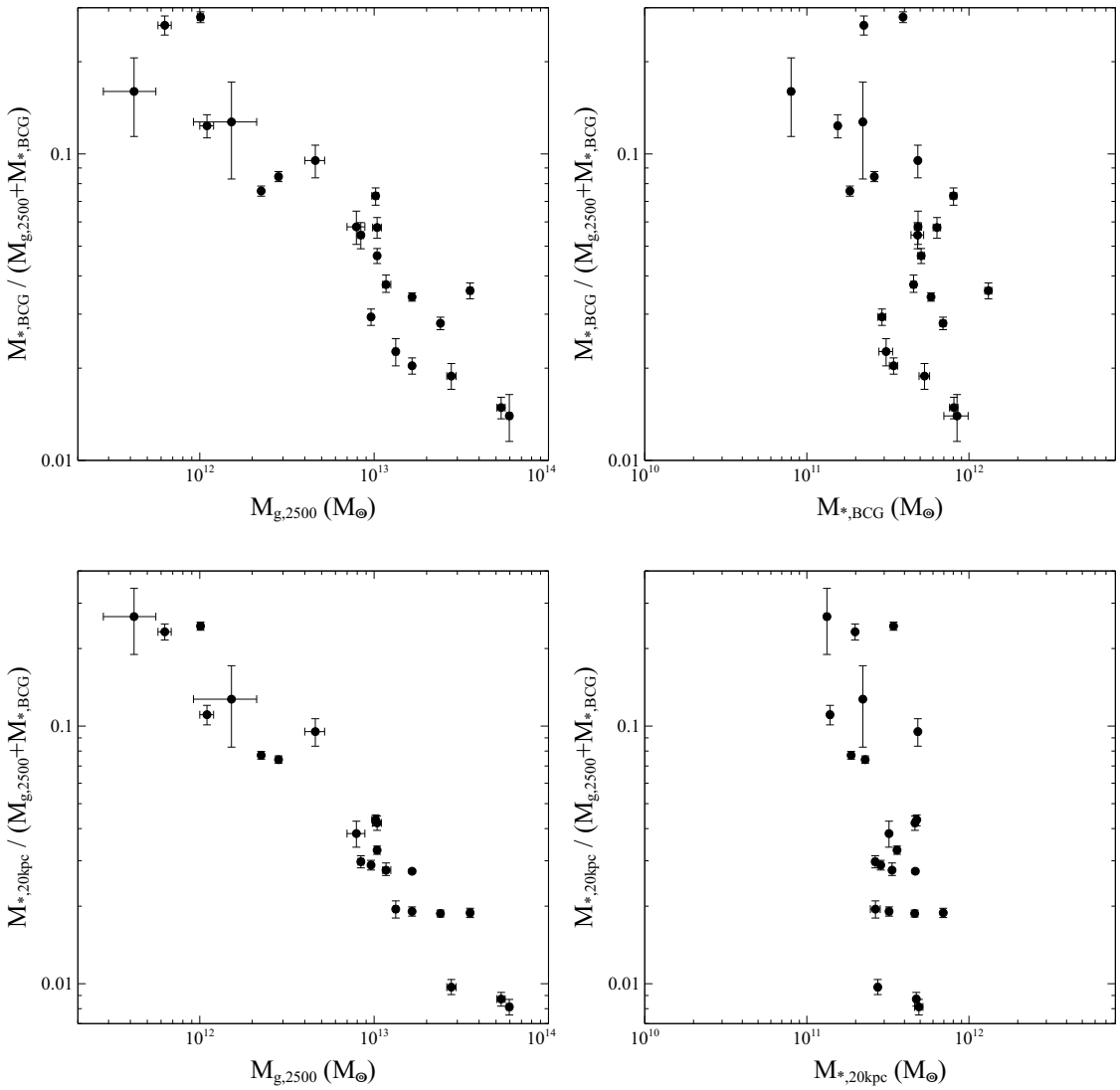

Figure 6. Top: $M_{*,\rm BCG}/(M_{g,2500}+M_{*,\rm BCG})$ vs. $\rm M_{g,2500}$ (*left*), $M_{*,\rm BCG}/(M_{g,2500}+M_{*,\rm BCG})$ vs. $\rm M_{*,BCG}$ (*right*). Bottom: Same as above, but with stellar mass calculated at 20kpc.

& Birnboim 2006). However, one or more additional mechanisms are need to suppress cooling, possibly including thermal conduction (Voigt & Fabian 2004) and AGN feedback (McNamara & Nulsen 2007). Figure 7 shows that heating has been remarkably efficient over the half the age of the universe (Ma et al. 2011; Ma, McNamara & Nulsen 2013; McDonald et al. 2013). BCGs have apparently grown by less than a factor of two in stellar mass since $z \sim 1$, driven primarily by mergers (Lidman et al. 2012, 2013) rather than cooling.

4.4 Accretion Rate

The analytic scaling between cavity energy and halo mass discussed above in section 4.3 assumes the accretion rate is a low, fixed fraction of the Eddington rate. In this section, we investigate whether accretion rate is a constant function of mass in our sample.

As matter accretes onto the central SMBH, the binding energy released by the accreting mass will drive an outburst with some efficiency ϵ. Assuming that the X-ray cavities dominate the total energy output of the AGN, the accretion rate can be estimated as

$$\dot{M}_{\rm BH} = \frac{P_{\rm cav}}{\epsilon c^2}. \quad (9)$$

The maximum accretion rate in which gravity is balanced by radiation pressure from accretion is given by the Eddington accretion rate, which for a fully ionized plasma can be calculated as

$$\frac{\dot{M}_{\rm Edd}}{M_\odot} = \frac{2.2}{\epsilon'}\left(\frac{M_{\rm BH}}{10^9 M_\odot}\right). \quad (10)$$

In Figure 8 we plot $\dot{M}/\dot{M}_{\rm Edd}$ against halo mass, assuming $\epsilon = \epsilon'$. The accretion rates in our systems range between $10^{-5}\dot{M}_{\rm Edd}$ and $0.04\dot{M}_{\rm Edd}$, all well below the Eddington rate, as expected for radiatively inefficient accretion. The weak positive trend shown in Figure 8 is harder to interpret. Taken at face value, it implies that higher mass halos accrete

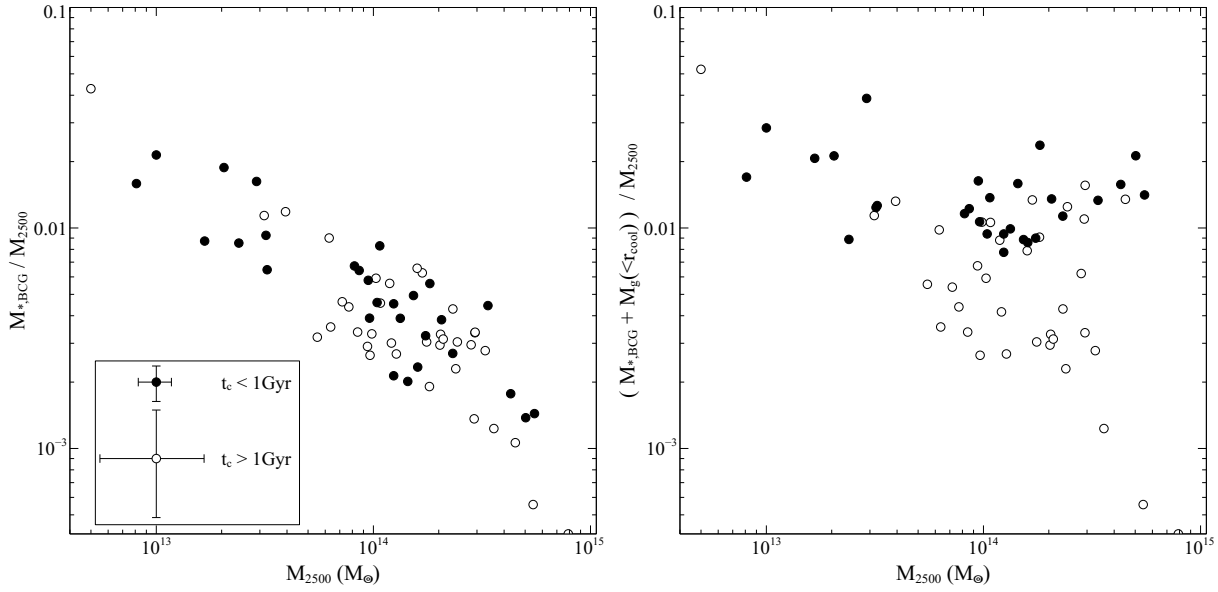

Figure 7. Left: $M_{*,BCG}/M_{2500}$ vs. M_{2500} in the full HIFLUGCS sample. Right: $(M_{*,BCG} + M_g(< r_{cool}))/M_{2500}$ vs. M_{2500}, representing the total possible stellar mass in the BCGs assuming cooling proceeds unimpeded. Systems are shown as either open or closed symbols based on the central cooling times from Hudson et al. (2010). The average size of the error bars is shown on the bottow left.

at higher specific accretion rates. However, the trend may be the result of incorrect underlying assumptions, such as misestimation of black hole masses. Explicitly, Figure 8 is a relationship between $P_{\rm cav}/L_K$ and M_{2500}. The estimates of $\dot{M}_{\rm Edd}$ rely on the scaling relation between $M_{\rm BH}$ and L_K. The black hole mass scaling relation is poorly constrained above $M_{\rm BH} \sim 10^9 M_\odot$ and data suggest an upturn to larger black hole masses (Lauer et al. 2007) in more massive galaxies (Graham & Scott 2015). Assuming accretion rate is indeed proportional to mass, in our sample, with $\dot{M}/\dot{M}_{\rm Edd} = 10^{-4}$, black hole masses exceeding $10^{10} M_\odot$ would be implied in the most massive clusters. Given M87's black hole mass of several 10^9 $M_\odot$ lies in a less luminous central galaxy, the existence of ultramassive black holes is plausible.

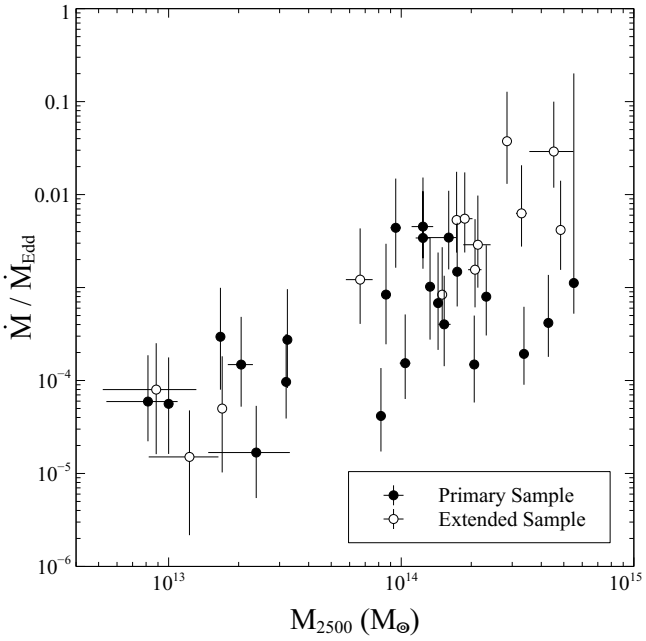

Figure 8. Accretion rate is compared to halo mass in our primary sample. Black hole masses are estimated from Graham (2007) using K-band luminosities derived from 2MASS, and $\dot{M}_{\rm BH}$ is estimated as $\dot{M}_{\rm BH} = P_{\rm cav}/\epsilon' c^2$.

5 AGN IN COOLING AND NON-COOLING ATMOSPHERES

5.1 Jet Power as a Function of Mass & Central Cooling Time

Earlier studies have suggested that AGN power may scale differently in cool and non-cool core systems. Mittal et al. (2009) found a correlation between the radio luminosity and the bolometric X-ray luminosity in cool-core systems, but no evidence for a correlation in weak or non cool-cores. In addition, Ma, McNamara & Nulsen (2013) found only a weak trend between *ROSAT* X-ray luminosity and NVSS radio luminosity, presumably including both cool core and non-cool core clusters. In this section we investigate the effects of AGN heating in the complete HIFLUGCS sample, which includes clusters with and without cool cores.

In order to examine the relationship between feedback in cooling and non-cooling atmospheres, we have separated the HIFLUGCS sample into systems with central cooling times above and below 1 Gyr. In all systems, we estimate the mechanical power from the central 1.4 GHz radio luminosity, using the relation from Cavagnolo et al. (2010)

$$\log P_{\rm mech} = 0.75\ (\pm 0.14) \log P_{1.4} + 1.91\ (\pm 0.18), \qquad (11)$$

where $P_{\rm mech}$ is in units of 10^{42} erg s^{-1} and $P_{1.4}$ is in units of 10^{40} erg s^{-1}. This relation has been measured over the full range of radio luminosities in our sample, and has a

scatter of 0.78 dex. Because many of our systems do not have well defined X-ray cavities and/or uniformly deep Chandra observations to detect them, applying the scaling relation to all systems yields uniform but somewhat higher variance over the sample. We refer to the power estimated using this relation as the "mechanical power", or $P_{\rm mech}$, throughout this section.

We plot the mechanical power against M_{2500} for the full HIFLUGCS sample in Figure 9. The distributions of $P_{\rm mech}$ for systems with short and long central atmospheric cooling times are segregated in Figure 9. Systems with central cooling times exceeding 1 Gyr experience AGN outbursts that are typically two orders of magnitude less powerful than systems with central cooling times below 1 Gyr. Systems with central cooling times less than 1 Gyr are not only more powerful, their AGN powers also correlate with halo mass. The correlation with halo mass is consistent with our earlier result using direct measurements of cavity power. In contrast, the AGN powers of systems with long central cooling times are not correlated with halo mass. Most are relatively weak or dormant. Nevertheless, some are experiencing powerful AGN outbursts that rival the most powerful in the entire sample.

We have superposed in Figure 9, our $P_{\rm cav}$-M_{2500} relation from section 4.3 and its 2σ lower limit to distinguish systems with high mechanical power for their halo mass. We find 11/36 ($\sim 30\%$) of the clusters with long cooling times lie above this limit, while all 28 of the clusters with short cooling times harbour powerful radio outbursts. In the latter, the AGN are presumably being fueled by cooling atmospheres, while the fueling mechanism in the clusters with long cooling times is unknown. Unresolved coronae (Sun 2009) or cold gas accreted from interloping galaxies (Hardcastle, Evans & Croston 2007) are candidates. This result shows heating from AGN is significant in all clusters, but systems with long central cooling times are not necessarily fueled by a feedback cycle.

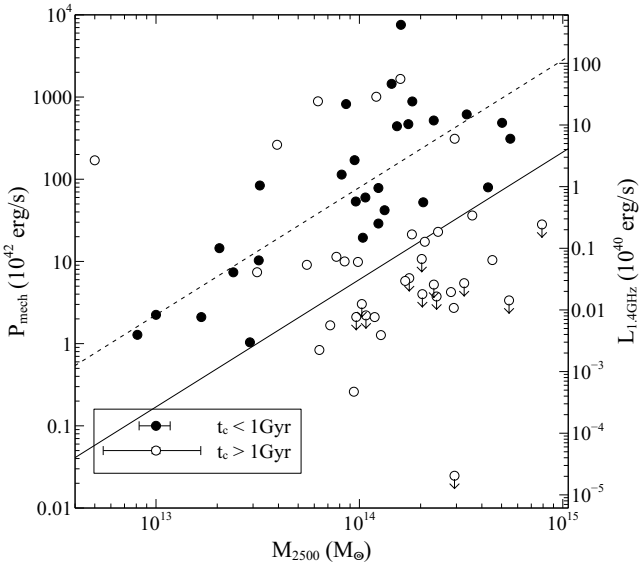

Figure 9. 1.4 GHz luminosity vs. M_{2500} in the full HIFLUGCS sample, with mechanical powers estimated using equation 11. Systems are shown as either open or closed symbols based on the central cooling times from Hudson et al. (2010). The dotted line is our best fit $P_{\rm mech}$-M_{2500} relation from section 4.3, and the solid line is the 2 σ lower limit on the relation. The average size of the error bars is shown at the bottom left. The average error on the 1.4GHz is smaller than the symbol size.

6 CONCLUSIONS

We derive X-ray mass, luminosity, and temperature profiles for 45 galaxy clusters to explore relationships between halo mass, AGN feedback, and central cooling time using the HIFLUGCS sample. We find that radio–mechanical feedback power, determined from X-ray cavities, correlates with halo mass, but only in halos with central atmospheric cooling times shorter than 1 Gyr. The 1 Gyr timescale corresponds approximately to the cooling time threshold for the onset of star formation (Rafferty, McNamara & Nulsen 2008) and the entropy threshold for Hα emission (Cavagnolo et al. 2008). For the HIFLUCGS sample, the relationship between cavity power and mass is of the form $P_{\rm cav} \propto M_{2500}^{1.55\pm0.26}$. No correlation is found in systems with central cooling times greater than 1 Gyr.

If cooling is regulated by AGN feedback fuelled by accretion at a fixed fraction of the Eddington rate, the trend of jet power with mass is expected to be $P_{\rm cav} \simeq L_{\rm cool} \sim M^{1.75}$, where the value of the exponent depends on the radial entropy profile and the mass dependence of the gas mass fraction, both of which are uncertain. This scaling is consistent with the observed trend between radio-mechanical power and halo mass.

The observed trend is also consistent with the assumption that jet power is proportional to black hole mass (Sijacki & Springel 2006; Somerville et al. 2008). This implies analytic scalings of $P_{\rm cav} \propto M^{4/3}$, for $M_{\rm BH} \propto \sigma^4$, or $P_{\rm cav} \propto M^{5/3}$, for $M_{\rm BH} \propto \sigma^5$. AGN power is correlated equally well with X-ray gas mass and total mass, but less well with the K-band luminosity of the central galaxy. Radio–mechanical powers in clusters with central atmospheric cooling times longer than $\sim$ 1 Gyr typically lie two orders of magnitude below those with shorter central cooling times. We find that $\sim 30\%$ of these clusters are experiencing radio outbursts comparable in power to the clusters with short central cooling times. This indicates that central galaxies undergo powerful radio outbursts regardless of their halo mass or central cooling time on the scales resolved in this study. Rare but powerful radio outbursts may well be the primary source of excess energy injected into the ICM.

We further investigate the impact of feedback on cluster scaling relations. We find $L-T$, and $M-T$ relations, excluding regions directly affected by AGN, with the forms $L \propto T^{2.63\pm0.10}$, $M \propto T^{1.87\pm0.12}$. These forms are consistent with the cluster population as a whole.

We examined the star formation history of central galaxies using the ratio of stellar mass (i.e., K-band luminosity) to total halo mass within R_{2500}. The fraction of the mass in the stars of the central galaxy decreases sharply with halo mass, consistent with David, Jones & Forman (1995) and Gonzalez et al. (2013). While the gas mass rises, the

stellar mass remains nearly constant with rising total mass. This trend is seen in all clusters regardless of central cooling time, which implies that star formation in central galaxies is tightly regulated throughout the buildup of their halos. It further implies a long-term balance between AGN heating and atmospheric cooling.

ACKNOWLEDGEMENTS

RAM, BRM and ANV acknowledge generous support from the Natural Sciences and Engineering Council of Canada. RAM and BRM acknowledge generous support from the Canadian Space Agency associated with the Astro-H project. PEJN was supported by NASA contract NAS8-03060.

The plots in this paper were created using VEUSZ[4]. This research has made use of data obtained from the Chandra Data Archive and the Chandra Source Catalog, and software provided by the Chandra X-ray Center (CXC) in the application packages CIAO, ChIPS, and Sherpa. This publication makes use of data products from the Two Micron All Sky Survey, which is a joint project of the University of Massachusetts and the Infrared Processing and Analysis Center/California Institute of Technology, funded by the National Aeronautics and Space Administration and the National Science Foundation. This research has made use of the NASA/IPAC Extragalactic Database (NED), which is operated by the Jet Propulsion Laboratory, California Institute of Technology, under contract with the National Aeronautics and Space Administration.

REFERENCES

Ade P. et al., 2013, arXiv preprint arXiv:1303.5076
Akritas M. G., Bershady M. A., 1996, ApJ, 470, 706
Alexander D. M., Hickox R. C., 2012, NewA Rev., 56, 93
Allen S. W., Dunn R. J. H., Fabian A. C., Taylor G. B., Reynolds C. S., 2006, MNRAS, 372, 21
Allen S. W., Rapetti D. A., Schmidt R. W., Ebeling H., Morris R. G., Fabian A. C., 2008, MNRAS, 383, 879
Anders E., Grevesse N., 1989, Geochim. Cosmochim. Acta, 53, 197
Arnaud K. A., 1996, in Astronomical Society of the Pacific Conference Series, Vol. 101, Astronomical Data Analysis Software and Systems V, Jacoby G. H., Barnes J., eds., p. 17
Arnaud M., Pointecouteau E., Pratt G. W., 2005, A&A, 441, 893
Babul A., Balogh M. L., Lewis G. F., Poole G. B., 2002, MNRAS, 330, 329
Balogh M. L., Navarro J. F., Morris S. L., 2000, ApJ, 540, 113
Batcheldor D., Marconi A., Merritt D., Axon D. J., 2007, ApJ, 663, L85
Behroozi P. S., Wechsler R. H., Conroy C., 2013, ApJ, 762, L31
Bell E. F., de Jong R. S., 2001, ApJ, 550, 212
Bernardi M., Meert A., Sheth R. K., Vikram V., Huertas-Company M., Mei S., Shankar F., 2013, MNRAS, 436, 697
Best P. N., von der Linden A., Kauffmann G., Heckman T. M., Kaiser C. R., 2007, MNRAS, 379, 894
Bialek J. J., Evrard A. E., Mohr J. J., 2001, ApJ, 555, 597
Bîrzan L., Rafferty D. A., McNamara B. R., Wise M. W., Nulsen P. E. J., 2004, ApJ, 607, 800
Bîrzan L., Rafferty D. A., Nulsen P. E. J., McNamara B. R., Röttgering H. J. A., Wise M. W., Mittal R., 2012, MNRAS, 427, 3468
Blanton E. L., Randall S. W., Clarke T. E., Sarazin C. L., McNamara B. R., Douglass E. M., McDonald M., 2011, ApJ, 737, 99
Bluck A. F. L., Mendel J. T., Ellison S. L., Moreno J., Simard L., Patton D. R., Starkenburg E., 2014, MNRAS, 441, 599
Bower R. G., Benson A. J., Malbon R., Helly J. C., Frenk C. S., Baugh C. M., Cole S., Lacey C. G., 2006, MNRAS, 370, 645
Burke C., Hilton M., Collins C., 2015, MNRAS, 449, 2353
Cavagnolo K. W., Donahue M., Voit G. M., Sun M., 2008, ApJ, 683, L107
Cavagnolo K. W., Donahue M., Voit G. M., Sun M., 2009, ApJS, 182, 12
Cavagnolo K. W., McNamara B. R., Nulsen P. E. J., Carilli C. L., Jones C., Bîrzan L., 2010, ApJ, 720, 1066
Churazov E., Brüggen M., Kaiser C. R., Böhringer H., Forman W., 2001, ApJ, 554, 261
Churazov E., Forman W., Jones C., Böhringer H., 2000, A&A, 356, 788
Croton D. J. et al., 2006, MNRAS, 365, 11
David L. P., Jones C., Forman W., 1995, ApJ, 445, 578
De Grandi S., Molendi S., 2001, ApJ, 551, 153
Dekel A., Birnboim Y., 2006, MNRAS, 368, 2
Dong R., Rasmussen J., Mulchaey J. S., 2010, ApJ, 712, 883
Dunn R. J. H., Fabian A. C., 2006, MNRAS, 373, 959
Dunn R. J. H., Fabian A. C., Taylor G. B., 2005, MNRAS, 364, 1343
Ebeling H., Edge A. C., Henry J. P., 2001, ApJ, 553, 668
Eckmiller H. J., Hudson D. S., Reiprich T. H., 2011, A&A, 535, A105
Edge A. C., 2001, MNRAS, 328, 762
Edge A. C., Stewart G. C., Fabian A. C., Arnaud K. A., 1990, MNRAS, 245, 559
Evrard A. E., Henry J. P., 1991, ApJ, 383, 95
Fabian A. C., 1994, ARA&A, 32, 277
Fabian A. C., 2012, ARA&A, 50, 455
Ferrarese L., 2002, ApJ, 578, 90
Ferrarese L., Merritt D., 2000, ApJ, 539, L9
Forman W. et al., 2007, ApJ, 665, 1057
Foster A. R., Ji L., Smith R. K., Brickhouse N. S., 2012, ApJ, 756, 128
Freeman P. E., Kashyap V., Rosner R., Lamb D. Q., 2002, ApJS, 138, 185
Gaspari M., Brighenti F., Temi P., Ettori S., 2014, ArXiv e-prints
Gebhardt K. et al., 2000, ApJ, 539, L13
Giodini S., Lovisari L., Pointecouteau E., Ettori S., Reiprich T. H., Hoekstra H., 2013, Space Sci. Rev., 177, 247

[4] http://home.gna.org/veusz/

Giodini S. et al., 2010, ApJ, 714, 218
Gitti M., McNamara B. R., Nulsen P. E. J., Wise M. W., 2007, ApJ, 660, 1118
Gonzalez A. H., Sivanandam S., Zabludoff A. I., Zaritsky D., 2013, ApJ, 778, 14
Gonzalez A. H., Zaritsky D., Zabludoff A. I., 2007, ApJ, 666, 147
Graham A. W., 2007, MNRAS, 379, 711
Graham A. W., Scott N., 2015, ApJ, 798, 54
Hardcastle M. J., Evans D. A., Croston J. H., 2007, MNRAS, 376, 1849
Heckman T. M., Best P. N., 2014, ARA&A, 52, 589
Hlavacek-Larrondo J. et al., 2013, ApJ, 777, 163
Hlavacek-Larrondo J., Fabian A. C., Edge A. C., Ebeling H., Sanders J. S., Hogan M. T., Taylor G. B., 2012, MNRAS, 421, 1360
Hudson D. S., Mittal R., Reiprich T. H., Nulsen P. E. J., Andernach H., Sarazin C. L., 2010, A&A, 513, A37
Israel H., Reiprich T. H., Erben T., Massey R. J., Sarazin C. L., Schneider P., Vikhlinin A., 2014, A&A, 564, A129
Kaiser N., 1986, MNRAS, 222, 323
Kaiser N., 1991, ApJ, 383, 104
Kalberla P. M. W., Burton W. B., Hartmann D., Arnal E. M., Bajaja E., Morras R., Pöppel W. G. L., 2005, A&A, 440, 775
Kirkpatrick C. C., McNamara B. R., 2015, MNRAS, 452, 4361
Kirkpatrick C. C., McNamara B. R., Cavagnolo K. W., 2011, ApJ, 731, L23
Kormendy J., Ho L. C., 2013, ARA&A, 51, 511
Kravtsov A., Vikhlinin A., Meshscheryakov A., 2014, ArXiv e-prints
Kravtsov A. V., Borgani S., 2012, ARA&A, 50, 353
Lauer T. R. et al., 2007, ApJ, 662, 808
Lidman C. et al., 2013, MNRAS, 433, 825
Lidman C. et al., 2012, MNRAS, 427, 550
Ma C.-J., McNamara B. R., Nulsen P. E. J., 2013, ApJ, 763, 63
Ma C.-J., McNamara B. R., Nulsen P. E. J., Schaffer R., Vikhlinin A., 2011, ApJ, 740, 51
Mahdavi A., Hoekstra H., Babul A., Bildfell C., Jeltema T., Henry J. P., 2013, ApJ, 767, 116
Mantz A., Allen S. W., Ebeling H., Rapetti D., Drlica-Wagner A., 2010, MNRAS, 406, 1773
Markevitch M., 1998, ApJ, 504, 27
Maughan B. J., Giles P. A., Randall S. W., Jones C., Forman W. R., 2012, MNRAS, 421, 1583
McCarthy I. G. et al., 2010, MNRAS, 406, 822
McConnell N. J., Ma C.-P., 2013, ApJ, 764, 184
McDonald M. et al., 2013, ApJ, 774, 23
McDonald M. et al., 2015, ArXiv e-prints
McNamara B. R., Nulsen P. E. J., 2007, ARA&A, 45, 117
McNamara B. R., Nulsen P. E. J., 2012, New Journal of Physics, 14, 055023
McNamara B. R., Nulsen P. E. J., Wise M. W., Rafferty D. A., Carilli C., Sarazin C. L., Blanton E. L., 2005, Nat, 433, 45
McNamara B. R. et al., 2014, ArXiv e-prints
McNamara B. R. et al., 2000, ApJ, 534, L135
Mendygral P. J., Jones T. W., Dolag K., 2012, ApJ, 750, 166
Mittal R., Hudson D. S., Reiprich T. H., Clarke T., 2009, A&A, 501, 835
Morganti R., Oosterloo T. A., Oonk J. B. R., Frieswijk W., Tadhunter C. N., 2015, ArXiv e-prints
Nagai D., Kravtsov A. V., Vikhlinin A., 2007, ApJ, 668, 1
Navarro J. F., Frenk C. S., White S. D. M., 1997, ApJ, 490, 493
Nulsen P., Jones C., Forman W., Churazov E., McNamara B., David L., Murray S., 2009, in American Institute of Physics Conference Series, Vol. 1201, American Institute of Physics Conference Series, Heinz S., Wilcots E., eds., pp. 198–201
Nulsen P. E. J., Hambrick D. C., McNamara B. R., Rafferty D., Birzan L., Wise M. W., David L. P., 2005, ApJ, 625, L9
Nulsen P. E. J., Powell S. L., Vikhlinin A., 2010, ApJ, 722, 55
O'Sullivan E., Giacintucci S., David L. P., Gitti M., Vrtilek J. M., Raychaudhury S., Ponman T. J., 2011, ApJ, 735, 11
Panagoulia E. K., Fabian A. C., Sanders J. S., 2014, MNRAS, 438, 2341
Paturel G., Petit C., Prugniel P., Theureau G., Rousseau J., Brouty M., Dubois P., Cambrésy L., 2003, A&A, 412, 45
Planelles S., Borgani S., Dolag K., Ettori S., Fabjan D., Murante G., Tornatore L., 2013, MNRAS, 431, 1487
Poggianti B. M., 1997, A&AS, 122, 399
Pointecouteau E., Arnaud M., Pratt G. W., 2005, A&A, 435, 1
Rafferty D. A., McNamara B. R., Nulsen P. E. J., 2008, ApJ, 687, 899
Rafferty D. A., McNamara B. R., Nulsen P. E. J., Wise M. W., 2006, ApJ, 652, 216
Randall S. W. et al., 2011, ApJ, 726, 86
Reiprich T. H., Böhringer H., 2002, ApJ, 567, 716
Russell H. R., McNamara B. R., Edge A. C., Hogan M. T., Main R. A., Vantyghem A. N., 2013, MNRAS, 432, 530
Russell H. R. et al., 2014, ApJ, 784, 78
Salomé P., Combes F., 2003, A&A, 412, 657
Sanders J. S., Fabian A. C., Allen S. W., Schmidt R. W., 2004, MNRAS, 349, 952
Sanders J. S., Fabian A. C., Taylor G. B., 2009, MNRAS, 393, 71
Schlafly E. F., Finkbeiner D. P., 2011, ApJ, 737, 103
Schlegel D. J., Finkbeiner D. P., Davis M., 1998, ApJ, 500, 525
Schmidt R. W., Allen S. W., 2007, MNRAS, 379, 209
Short C. J., Thomas P. A., Young O. E., Pearce F. R., Jenkins A., Muanwong O., 2010, MNRAS, 408, 2213
Shurkin K., Dunn R. J. H., Gentile G., Taylor G. B., Allen S. W., 2008, MNRAS, 383, 923
Sijacki D., Springel V., 2006, MNRAS, 366, 397
Silk J., Rees M. J., 1998, A&A, 331, L1
Simionescu A., Werner N., Finoguenov A., Böhringer H., Brüggen M., 2008, A&A, 482, 97
Skrutskie M. F. et al., 2006, AJ, 131, 1163
Somerville R. S., Hopkins P. F., Cox T. J., Robertson B. E., Hernquist L., 2008, MNRAS, 391, 481
Sun M., 2009, ApJ, 704, 1586
Sun M., Jones C., Forman W., Vikhlinin A., Donahue M., Voit M., 2007, ApJ, 657, 197

Tozzi P., Norman C., 2001, ApJ, 546, 63
Tremaine S. et al., 2002, ApJ, 574, 740
van Dokkum P. G., Franx M., 2001, ApJ, 553, 90
Vantyghem A. N., McNamara B. R., Russell H. R., Main R. A., Nulsen P. E. J., Wise M. W., Hoekstra H., Gitti M., 2014, MNRAS, 442, 3192
Vikhlinin A. et al., 2009, ApJ, 692, 1033
Vikhlinin A., Kravtsov A., Forman W., Jones C., Markevitch M., Murray S. S., Van Speybroeck L., 2006, ApJ, 640, 691
Vikhlinin A., Markevitch M., Murray S. S., Jones C., Forman W., Van Speybroeck L., 2005, ApJ, 628, 655
Voigt L. M., Fabian A. C., 2004, MNRAS, 347, 1130
Voit G. M., Balogh M. L., Bower R. G., Lacey C. G., Bryan G. L., 2003, ApJ, 593, 272
Voit G. M., Kay S. T., Bryan G. L., 2005, MNRAS, 364, 909
Wu K. K. S., Fabian A. C., Nulsen P. E. J., 2000, MNRAS, 318, 889
Zhang Y.-Y., Finoguenov A., Böhringer H., Kneib J.-P., Smith G. P., Kneissl R., Okabe N., Dahle H., 2008, A&A, 482, 451

APPENDIX A: MASS PROFILES

Here we present our derived mass profiles:

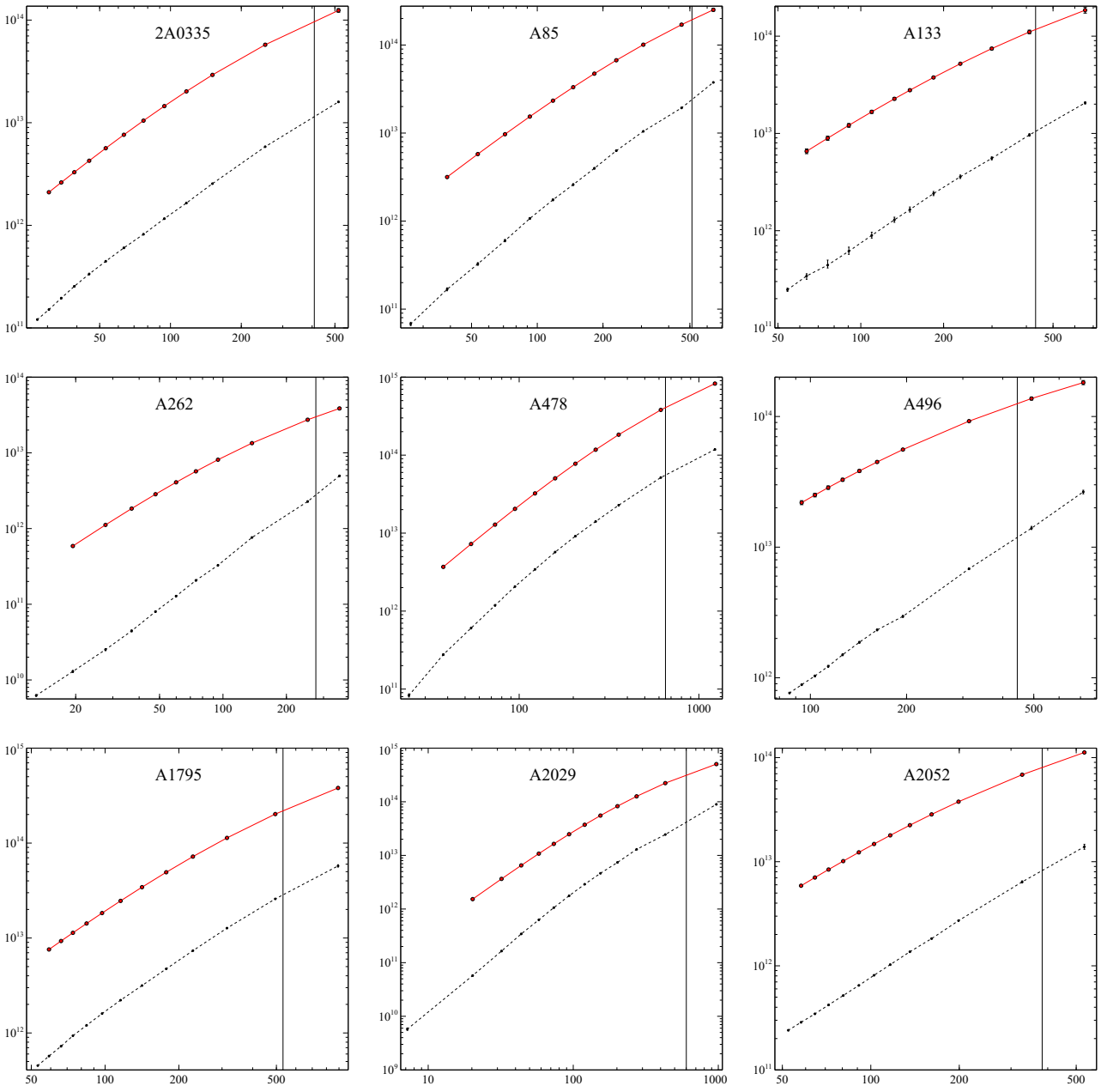

Figure A1. Mass profiles of total and gas mass. The y axis gives the enclosed mass in $M_{\odot}$, the x-axis gives the radius from the cluster centre in kpc. The red curve denotes the total mass profile, and the dashed black curve is the gas mass profile. The solid vertical line denotes R_{2500}. Note that the error bars in each profile are correlated.

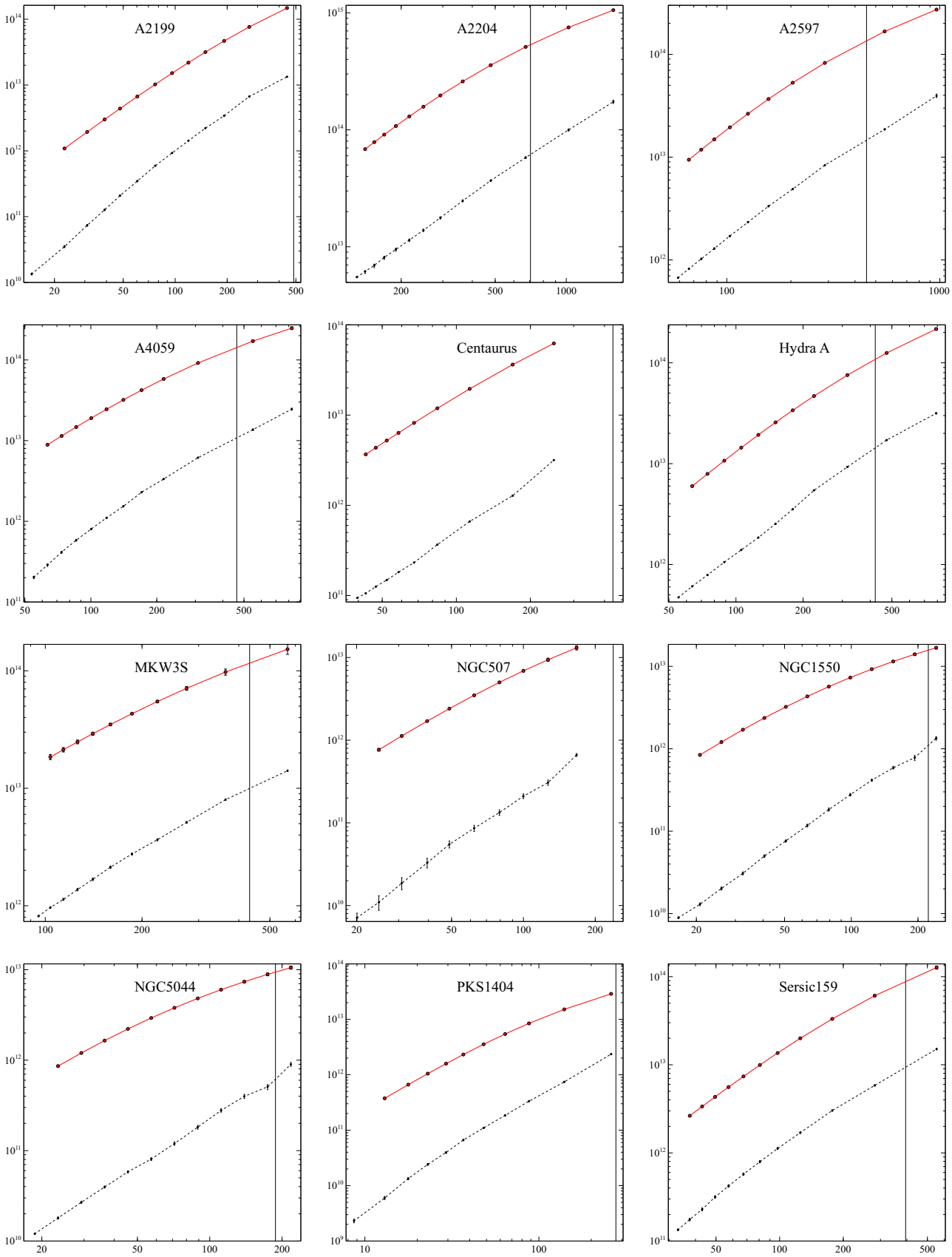

Figure A2. Continued from figure A1

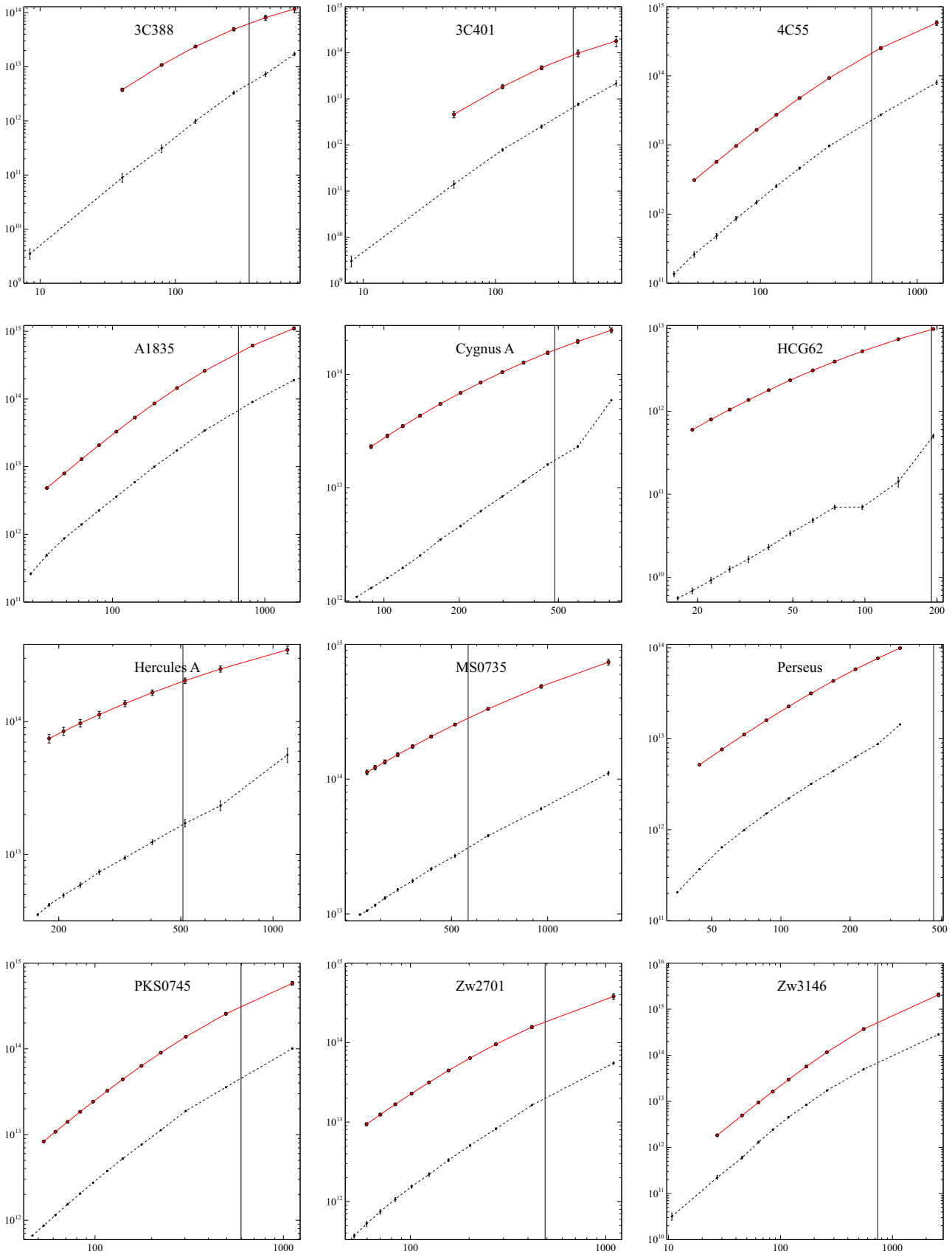

Figure A3. Continued from figure A1

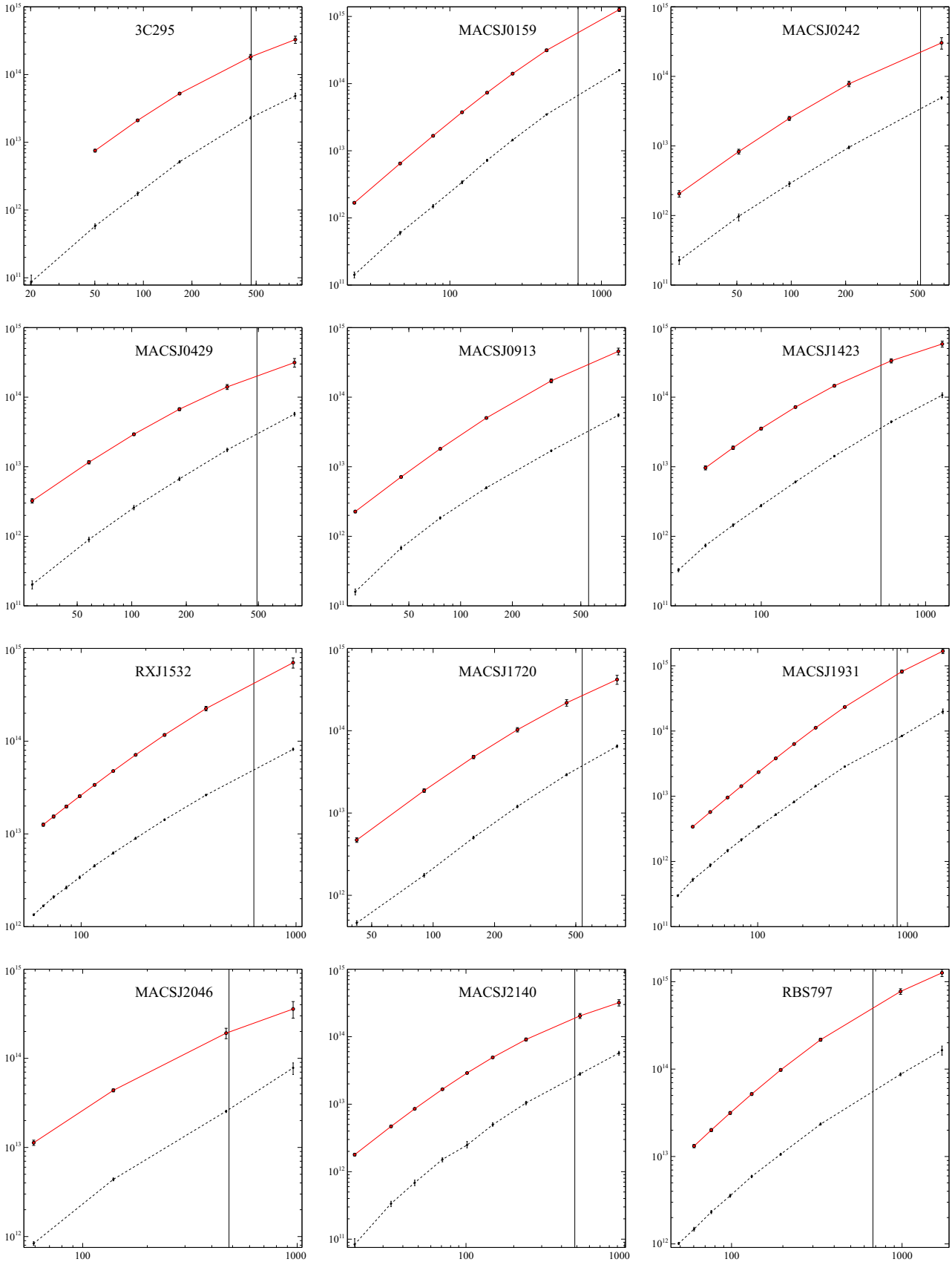

Figure A4. Continued from figure A1

Table A1: Derived Mass Profiles

$A = 4\pi G\rho_0 r_s^2 \mu m_H$ is in units of keV, R_s is given in units of kpc

2A0335	r (kpc)	27.2	30.4	34.3	39.0	45.1	53.1	63.4	76.8	94.2	116.8	150.8	252.8	517.8
$\rho_o = 31.0^{2.6}_{-2.1}$	M_g (10^{11} $M_\odot$)	$1.21^{0.014}_{-0.014}$	$1.51^{0.022}_{-0.022}$	$1.95^{0.031}_{-0.031}$	$2.55^{0.04}_{-0.04}$	$3.36^{0.05}_{-0.05}$	$4.47^{0.064}_{-0.063}$	$6.03^{0.08}_{-0.079}$	$8.18^{0.1}_{-0.1}$	$11.6^{0.13}_{-0.13}$	$16.5^{0.17}_{-0.17}$	$25.5^{0.23}_{-0.23}$	$58.3^{0.47}_{-0.47}$	$159.0^{2.1}_{-2.1}$
$R_s = 204.0^{28.0}_{-22.0}$	M (10^{13} $M_\odot$)	-	0.21 ± 0.0025	0.262 ± 0.0028	0.329 ± 0.0032	0.426 ± 0.0035	0.564 ± 0.0037	0.763 ± 0.0037	1.05 ± 0.0043	1.45 ± 0.0081	2.02 ± 0.018	2.92 ± 0.04	5.75 ± 0.14	12.4 ± 0.51
3C295	r (kpc)	20.2	50.2	92.1	167.7	462.4	875.0							
$\rho_o = 50.9^{9.9}_{-6.7}$	M_g (10^{13} $M_\odot$)	$0.00866^{0.0023}_{-0.0031}$	$0.0579^{0.0045}_{-0.0049}$	$0.174^{0.011}_{-0.011}$	$0.515^{0.02}_{-0.02}$	$2.3^{0.099}_{-0.099}$	$4.85^{0.47}_{-0.45}$							
$R_s = 236.0^{96.0}_{-64.0}$	M (10^{13} $M_\odot$)	-	0.75 ± 0.035	2.1 ± 0.073	5.2 ± 0.2	18.0 ± 1.6	33.0 ± 4.0							
3C388	r (kpc)	8.4	40.5	78.9	140.5	269.7	462.7	757.2						
$\rho_o = 23.7^{2.5}_{-1.5}$	M_g (10^{12} $M_\odot$)	$0.00351^{0.00081}_{-0.00072}$	$0.0896^{0.017}_{-0.016}$	$0.311^{0.047}_{-0.048}$	$0.989^{0.094}_{-0.096}$	$3.3^{0.23}_{-0.21}$	$7.31^{0.7}_{-0.68}$	$17.3^{1.3}_{-1.3}$						
$R_s = 127.0^{38.0}_{-27.0}$	M (10^{13} $M_\odot$)	-	0.38 ± 0.027	1.1 ± 0.045	2.4 ± 0.08	5.0 ± 0.35	8.1 ± 0.88	12.0 ± 1.7						
3C401	r (kpc)	8.1	48.5	113.2	223.0	420.7	816.2							
$\rho_o = 30.3^{13.0}_{-5.8}$	M_g (10^{12} $M_\odot$)	$0.00303^{0.00086}_{-0.00076}$	$0.141^{0.026}_{-0.026}$	$0.79^{0.051}_{-0.058}$	$2.53^{0.23}_{-0.23}$	$7.57^{0.53}_{-0.43}$	$21.7^{3.2}_{-2.7}$							
$R_s = 210.0^{180.0}_{-82.0}$	M (10^{13} $M_\odot$)	-	0.5 ± 0.073	2.0 ± 0.19	5.0 ± 0.47	10.0 ± 1.6	20.0 ± 4.6							
A85	r (kpc)	26.3	38.6	53.4	71.2	92.4	118.0	146.1	182.6	230.1	306.1	458.0	640.4	
$\rho_o = 51.1^{5.0}_{-4.0}$	M_g (10^{12} $M_\odot$)	$0.0679^{0.0029}_{-0.0029}$	$0.168^{0.0065}_{-0.0064}$	$0.326^{0.011}_{-0.011}$	$0.6^{0.018}_{-0.018}$	$1.07^{0.027}_{-0.026}$	$1.74^{0.039}_{-0.039}$	$2.6^{0.054}_{-0.054}$	$3.97^{0.074}_{-0.073}$	$6.3^{0.095}_{-0.095}$	$10.5^{0.13}_{-0.13}$	$19.3^{0.29}_{-0.29}$	$37.6^{0.46}_{-0.46}$	
$R_s = 381.0^{66.0}_{-53.0}$	M (10^{13} $M_\odot$)	-	0.32 ± 0.0057	0.58 ± 0.0089	0.97 ± 0.012	1.5 ± 0.015	2.3 ± 0.018	3.3 ± 0.023	4.7 ± 0.04	6.7 ± 0.082	10.0 ± 0.18	17.0 ± 0.47	25.0 ± 0.9	
A133	r (kpc)	54.1	63.5	75.8	90.5	109.6	132.5	150.8	183.8	230.0	299.3	410.2	654.1	
$\rho_o = 36.4^{6.9}_{-3.6}$	M_g (10^{12} $M_\odot$)	$0.247^{0.0099}_{-0.0096}$	$0.343^{0.018}_{-0.026}$	$0.442^{0.056}_{-0.029}$	$0.615^{0.063}_{-0.044}$	$0.894^{0.071}_{-0.055}$	$1.29^{0.084}_{-0.074}$	$1.65^{0.1}_{-0.094}$	$2.41^{0.12}_{-0.11}$	$3.58^{0.15}_{-0.14}$	$5.54^{0.21}_{-0.2}$	$9.64^{0.3}_{-0.29}$	$20.6^{0.56}_{-0.56}$	
$R_s = 314.0^{130.0}_{-75.0}$	M (10^{13} $M_\odot$)	-	0.66 ± 0.037	0.89 ± 0.045	1.2 ± 0.053	1.7 ± 0.061	2.3 ± 0.066	2.8 ± 0.068	3.8 ± 0.07	5.2 ± 0.094	7.4 ± 0.2	11.0 ± 0.47	18.0 ± 1.2	
A1795	r (kpc)	53.1	59.0	66.1	73.9	84.0	97.2	115.7	141.5	177.6	228.2	314.2	494.9	892.2
$\rho_o = 55.0^{1.6}_{-1.6}$	M_g (10^{12} $M_\odot$)	$0.453^{0.003}_{-0.0035}$	$0.571^{0.0079}_{-0.0064}$	$0.724^{0.0097}_{-0.0088}$	$0.935^{0.012}_{-0.0094}$	$1.2^{0.013}_{-0.012}$	$1.6^{0.016}_{-0.014}$	$2.21^{0.019}_{-0.017}$	$3.16^{0.024}_{-0.023}$	$4.73^{0.032}_{-0.03}$	$7.36^{0.042}_{-0.041}$	$12.7^{0.06}_{-0.059}$	$25.8^{0.21}_{-0.22}$	$57.5^{1.7}_{-1.5}$
$R_s = 373.0^{21.0}_{-21.0}$	M (10^{13} $M_\odot$)	-	0.758 ± 0.0072	0.93 ± 0.0084	1.13 ± 0.0097	1.42 ± 0.011	1.83 ± 0.013	2.46 ± 0.015	3.43 ± 0.016	4.93 ± 0.016	7.2 ± 0.016	11.3 ± 0.044	20.2 ± 0.17	38.1 ± 0.54
A1835	r (kpc)	29.1	37.0	48.2	62.6	81.4	105.9	140.1	188.0	264.7	402.7	830.4	1550.8	
$\rho_o = 95.7^{3.4}_{-3.7}$	M_g (10^{12} $M_\odot$)	$0.262^{0.0074}_{-0.0073}$	$0.491^{0.013}_{-0.012}$	$0.867^{0.019}_{-0.018}$	$1.4^{0.028}_{-0.027}$	$2.25^{0.041}_{-0.041}$	$3.61^{0.059}_{-0.058}$	$5.89^{0.085}_{-0.085}$	$9.97^{0.12}_{-0.12}$	$17.3^{0.18}_{-0.18}$	$34.2^{0.32}_{-0.29}$	$90.4^{0.87}_{-0.86}$	$190.0^{3.2}_{-3.2}$	
$R_s = 439.0^{29.0}_{-31.0}$	M (10^{13} $M_\odot$)	-	0.48 ± 0.0099	0.79 ± 0.015	1.3 ± 0.022	2.1 ± 0.03	3.3 ± 0.039	5.3 ± 0.045	8.6 ± 0.052	14.0 ± 0.11	26.0 ± 0.4	62.0 ± 1.9	110.0 ± 4.9	
A2029	r (kpc)	7.2	20.3	32.0	43.8	57.9	73.4	93.6	119.9	154.0	201.8	273.4	431.1	969.7
$\rho_o = 68.8^{3.9}_{-3.4}$	M_g (10^{12} $M_\odot$)	$0.00577^{0.0003}_{-0.0003}$	$0.0575^{0.0015}_{-0.0015}$	$0.164^{0.0037}_{-0.0036}$	$0.343^{0.0062}_{-0.0062}$	$0.629^{0.01}_{-0.01}$	$1.06^{0.015}_{-0.015}$	$1.77^{0.021}_{-0.021}$	$2.9^{0.03}_{-0.03}$	$4.63^{0.044}_{-0.044}$	$7.4^{0.063}_{-0.063}$	$13.0^{0.091}_{-0.097}$	$24.5^{0.21}_{-0.21}$	$89.5^{1.1}_{-1.1}$
$R_s = 304.0^{30.0}_{-26.0}$	M (10^{13} $M_\odot$)	-	0.153 ± 0.0024	0.365 ± 0.005	0.651 ± 0.0079	1.08 ± 0.011	1.64 ± 0.014	2.48 ± 0.017	3.73 ± 0.02	5.53 ± 0.024	8.27 ± 0.044	12.6 ± 0.1	22.3 ± 0.3	50.4 ± 1.1
A2052	r (kpc)	52.4	57.9	64.5	71.8	80.6	91.1	102.6	116.4	135.8	161.0	198.8	327.4	533.0
$\rho_o = 27.3^{0.48}_{-0.46}$	M_g (10^{12} $M_\odot$)	$0.24^{0.0028}_{-0.0028}$	$0.287^{0.0033}_{-0.0032}$	$0.346^{0.0037}_{-0.0038}$	$0.421^{0.0043}_{-0.0043}$	$0.518^{0.005}_{-0.005}$	$0.648^{0.0059}_{-0.0059}$	$0.811^{0.0069}_{-0.0069}$	$1.03^{0.0082}_{-0.0081}$	$1.36^{0.0099}_{-0.0098}$	$1.82^{0.013}_{-0.013}$	$2.72^{0.017}_{-0.018}$	$6.4^{0.14}_{-0.14}$	$13.9^{0.78}_{-0.76}$
$R_s = 198.0^{9.7}_{-9.6}$	M (10^{13} $M_\odot$)	-	0.588 ± 0.0057	0.705 ± 0.0064	0.841 ± 0.0071	1.01 ± 0.0077	1.23 ± 0.0084	1.48 ± 0.0088	1.79 ± 0.0091	2.24 ± 0.0093	2.85 ± 0.0095	3.77 ± 0.012	6.85 ± 0.045	11.2 ± 0.12
A2199	r (kpc)	14.8	22.8	30.9	39.0	47.9	60.4	76.6	96.0	119.3	149.6	192.1	268.5	444.2
$\rho_o = 45.6^{2.8}_{-2.1}$	M_g (10^{11} $M_\odot$)	$0.135^{0.0048}_{-0.0047}$	$0.351^{0.013}_{-0.013}$	$0.738^{0.022}_{-0.021}$	$1.27^{0.032}_{-0.031}$	$2.08^{0.044}_{-0.044}$	$3.47^{0.061}_{-0.06}$	$5.93^{0.082}_{-0.081}$	$9.29^{0.11}_{-0.11}$	$14.3^{0.15}_{-0.14}$	$22.1^{0.19}_{-0.19}$	$34.1^{0.26}_{-0.26}$	$66.9^{0.34}_{-0.34}$	$134.0^{0.74}_{-0.74}$
$R_s = 363.0^{36.0}_{-26.0}$	M (10^{13} $M_\odot$)	-	0.109 ± 0.0013	0.194 ± 0.0021	0.3 ± 0.003	0.439 ± 0.0039	0.669 ± 0.005	1.02 ± 0.0061	1.52 ± 0.0067	2.19 ± 0.0069	3.17 ± 0.01	4.68 ± 0.024	7.64 ± 0.071	14.8 ± 0.24
A2204	r (kpc)	129.9	140.8	153.9	169.6	190.0	216.6	248.4	293.1	364.4	478.6	672.7	1022.2	1581.2
$\rho_o = 97.9^{3.6}_{-2.7}$	M_g (10^{13} $M_\odot$)	$0.55^{0.0051}_{-0.0046}$	$0.616^{0.0094}_{-0.025}$	$0.693^{0.018}_{-0.029}$	$0.811^{0.019}_{-0.03}$	$0.95^{0.022}_{-0.032}$	$1.14^{0.024}_{-0.032}$	$1.39^{0.03}_{-0.036}$	$1.77^{0.035}_{-0.041}$	$2.47^{0.05}_{-0.052}$	$3.68^{0.064}_{-0.065}$	$5.79^{0.1}_{-0.1}$	$9.98^{0.2}_{-0.2}$	$17.4^{0.56}_{-0.56}$
$R_s = 305.0^{54.0}_{-45.0}$	M (10^{14} $M_\odot$)	-	0.684 ± 0.0077	0.785 ± 0.0086	0.91 ± 0.0097	1.08 ± 0.011	1.3 ± 0.013	1.58 ± 0.015	1.97 ± 0.018	2.59 ± 0.023	3.57 ± 0.031	5.11 ± 0.046	7.51 ± 0.076	10.5 ± 0.12
A2597	r (kpc)	59.0	66.4	75.9	87.3	103.3	125.7	157.0	204.0	288.6	551.0	965.5		
$\rho_o = 39.1^{1.3}_{-1.5}$	M_g (10^{12} $M_\odot$)	$0.671^{0.0051}_{-0.0051}$	$0.819^{0.01}_{-0.01}$	$1.02^{0.015}_{-0.015}$	$1.29^{0.02}_{-0.02}$	$1.71^{0.025}_{-0.025}$	$2.33^{0.033}_{-0.033}$	$3.33^{0.043}_{-0.043}$	$4.89^{0.058}_{-0.058}$	$8.34^{0.081}_{-0.08}$	$18.6^{0.28}_{-0.28}$	$39.5^{1.5}_{-1.5}$		
$R_s = 234.0^{20.0}_{-25.0}$	M (10^{13} $M_\odot$)	-	0.943 ± 0.014	1.18 ± 0.016	1.49 ± 0.019	1.95 ± 0.021	2.64 ± 0.023	3.68 ± 0.024	5.3 ± 0.021	8.26 ± 0.032	16.7 ± 0.18	27.3 ± 0.45		
A262	r (kpc)	13.0	19.4	27.7	36.8	47.8	59.9	74.4	94.7	137.3	252.3	357.2		
$\rho_o = 14.0^{0.52}_{-0.45}$	M_g (10^{11} $M_\odot$)	$0.0624^{0.0016}_{-0.0016}$	$0.13^{0.004}_{-0.004}$	$0.252^{0.0079}_{-0.0079}$	$0.445^{0.013}_{-0.013}$	$0.799^{0.019}_{-0.019}$	$1.28^{0.028}_{-0.028}$	$2.07^{0.04}_{-0.04}$	$3.27^{0.064}_{-0.064}$	$7.62^{0.11}_{-0.11}$	$22.8^{0.41}_{-0.4}$	$49.6^{0.8}_{-0.79}$		
$R_s = 134.0^{11.0}_{-9.7}$	M (10^{12} $M_\odot$)	-	0.59 ± 0.012	1.1 ± 0.02	1.8 ± 0.027	2.8 ± 0.033	4.1 ± 0.034	5.7 ± 0.032	8.1 ± 0.034	13.0 ± 0.12	27.0 ± 0.57	39.0 ± 1.1		
A4059	r (kpc)	54.9	63.4	73.5	85.7	100.3	117.9	140.7	170.4	214.9	308.3	549.1	825.9	
$\rho_o = 40.2^{1.7}_{-1.5}$	M_g (10^{12} $M_\odot$)	$0.203^{0.0058}_{-0.0084}$	$0.288^{0.0085}_{-0.012}$	$0.415^{0.011}_{-0.013}$	$0.583^{0.014}_{-0.016}$	$0.803^{0.017}_{-0.019}$	$1.1^{0.022}_{-0.023}$	$1.54^{0.028}_{-0.029}$	$2.29^{0.034}_{-0.035}$	$3.34^{0.047}_{-0.048}$	$6.15^{0.081}_{-0.081}$	$13.7^{0.3}_{-0.3}$	$24.6^{0.71}_{-0.73}$	
$R_s = 237.0^{29.0}_{-25.0}$	M (10^{13} $M_\odot$)	-	0.89 ± 0.019	1.1 ± 0.021	1.5 ± 0.024	1.9 ± 0.025	2.4 ± 0.025	3.2 ± 0.022	4.2 ± 0.02	5.8 ± 0.041	9.2 ± 0.14	17.0 ± 0.49	25.0 ± 0.92	
A478	r (kpc)	24.4	37.8	54.0	73.4	94.8	122.5	158.6	205.5	266.4	357.9	613.9	1228.5	
$\rho_o = 86.7^{6.6}_{-5.5}$	M_g (10^{12} $M_\odot$)	$0.0831^{0.0039}_{-0.0038}$	$0.277^{0.0075}_{-0.0075}$	$0.606^{0.014}_{-0.014}$	$1.18^{0.023}_{-0.023}$	$2.07^{0.034}_{-0.034}$	$3.43^{0.049}_{-0.049}$	$5.71^{0.069}_{-0.069}$	$9.14^{0.099}_{-0.099}$	$14.1^{0.14}_{-0.14}$	$22.8^{0.21}_{-0.21}$	$51.6^{0.5}_{-0.5}$	$118.0^{2.8}_{-2.8}$	
$R_s = 553.0^{68.0}_{-56.0}$	M (10^{13} $M_\odot$)	-	0.37 ± 0.0059	0.73 ± 0.011	1.3 ± 0.017	2.0 ± 0.024	3.2 ± 0.032	5.0 ± 0.044	7.8 ± 0.063	12.0 ± 0.1	18.0 ± 0.21	38.0 ± 0.74	83.0 ± 2.6	
A496	r (kpc)	86.0	93.9	103.3	113.7	126.2	142.3	161.8	194.8	313.6	491.9	714.4		
$\rho_o = 37.9^{0.66}_{-0.62}$	M_g (10^{12} $M_\odot$)	$0.765^{0.0065}_{-0.0064}$	$0.884^{0.011}_{-0.011}$	$1.03^{0.016}_{-0.016}$	$1.22^{0.02}_{-0.02}$	$1.5^{0.024}_{-0.024}$	$1.87^{0.029}_{-0.029}$	$2.33^{0.034}_{-0.035}$	$2.95^{0.053}_{-0.053}$	$6.83^{0.11}_{-0.1}$	$14.0^{0.46}_{-0.31}$	$26.5^{0.78}_{-0.91}$		
$R_s = 131.0^{26.0}_{-21.0}$	M (10^{13} $M_\odot$)	-	2.2 ± 0.078	2.5 ± 0.081	2.9 ± 0.084	3.3 ± 0.085	3.8 ± 0.085	4.5 ± 0.082	5.6 ± 0.075	9.2 ± 0.13	14.0 ± 0.36	18.0 ± 0.66		
Centaurus	r (kpc)	39.6	42.9	47.1	52.1	58.2	67.3	83.8	113.3	169.4	249.0			
$\rho_o = 35.1^{0.27}_{-0.38}$	M_g (10^{11} $M_\odot$)	$0.944^{0.0047}_{-0.0047}$	$1.06^{0.0079}_{-0.0078}$	$1.26^{0.011}_{-0.011}$	$1.49^{0.014}_{-0.014}$	$1.82^{0.018}_{-0.018}$	$2.32^{0.026}_{-0.026}$	$3.67^{0.035}_{-0.035}$	$6.63^{0.053}_{-0.053}$	$12.8^{0.13}_{-0.13}$	$31.7^{0.21}_{-0.21}$			
$R_s = 276.0$	M (10^{12} $M_\odot$)	-	3.67 ± 0.034	4.35 ± 0.04	5.22 ± 0.048	6.35 ± 0.059	8.19 ± 0.076	11.9 ± 0.11	19.5 ± 0.18	36.3 ± 0.34	62.3 ± 0.57			
Cygnus A	r (kpc)	77.8	88.8	103.2	119.0	139.5	168.3	202.8	244.2	298.0	362.6	453.0	597.7	814.7
$\rho_o = 45.2^{4.5}_{-2.1}$	M_g (10^{12} $M_\odot$)	$1.09^{0.0047}_{-0.0024}$	$1.3^{0.0083}_{-0.016}$	$1.59^{0.016}_{-0.021}$	$1.96^{0.025}_{-0.028}$	$2.52^{0.033}_{-0.036}$	$3.49^{0.042}_{-0.044}$	$4.59^{0.057}_{-0.059}$	$6.2^{0.066}_{-0.073}$	$8.37^{0.097}_{-0.1}$	$11.3^{0.17}_{-0.17}$	$16.0^{0.27}_{-0.26}$	$23.1^{0.55}_{-0.54}$	$59.0^{0.65}_{-0.64}$
$R_s = 145.0^{70.0}_{-43.0}$	M (10^{13} $M_\odot$)	-	2.3 ± 0.087	2.9 ± 0.094	3.5 ± 0.099	4.3 ± 0.1	5.5 ± 0.1	6.9 ± 0.11	8.5 ± 0.13	10.0 ± 0.21	13.0 ± 0.32	16.0 ± 0.5	20.0 ± 0.79	25.0 ± 1.2
HCG62	r (kpc)	16.5	19.0	22.8	27.3	32.6	39.6	48.7	60.6	74.8	97.5	137.8	192.9	
$\rho_o = 7.02^{1.9}_{-0.8}$	M_g (10^{10} $M_\odot$)	$0.558^{0.024}_{-0.024}$	$0.688^{0.053}_{-0.053}$	$0.918^{0.073}_{-0.074}$	$1.25^{0.097}_{-0.097}$	$1.65^{0.13}_{-0.13}$	$2.3^{0.17}_{-0.17}$	$3.39^{0.21}_{-0.21}$	$4.86^{0.28}_{-0.28}$	$7.0^{0.39}_{-0.39}$	$7.0^{0.39}_{-0.39}$	$14.2^{1.8}_{-1.9}$	$50.3^{2.9}_{-2.9}$	
$R_s = 48.6^{37.0}_{-19.0}$	M (10^{12} $M_\odot$)	-	0.6 ± 0.011	0.8 ± 0.014	1.1 ± 0.017	1.4 ± 0.021	1.8 ± 0.025	2.4 ± 0.029	3.1 ± 0.034	4.0 ± 0.04	5.3 ± 0.056	7.4 ± 0.11	9.8 ± 0.21	
Hercules A	r (kpc)	170.8	186.0	207.3	235.1	271.1	328.8	403.8	516.3	673.8	1114.7			
$\rho_o = 53.7^{14.0}_{-3.4}$	M_g (10^{13} $M_\odot$)	$0.352^{0.0054}_{-0.0054}$	$0.419^{0.01}_{-0.012}$	$0.494^{0.015}_{-0.017}$	$0.589^{0.023}_{-0.023}$	$0.738^{0.028}_{-0.029}$	$0.945^{0.032}_{-0.033}$	$1.24^{0.056}_{-0.052}$	$1.72^{0.12}_{-0.1}$	$2.33^{0.2}_{-0.18}$	$5.62^{0.69}_{-0.7}$			

$R_s = 135.0^{190.0}_{-85.0}$	M (10^{14} $M_\odot$)	-	0.75±0.056	0.85±0.059	0.97±0.063	1.1±0.066	1.4±0.072	1.7±0.08	2.0±0.098	2.5±0.13	3.5±0.23			
Hydra A	r (kpc)	55.3	63.6	74.5	88.7	105.6	126.0	150.5	179.8	223.8	315.9	473.8	789.7	
$\rho_o = 35.3^{1.2}_{-0.65}$	M_g (10^{12} $M_\odot$)	$0.472^{0.0025}_{-0.0025}$	$0.607^{0.005}_{-0.005}$	$0.787^{0.0077}_{-0.0076}$	$1.06^{0.011}_{-0.011}$	$1.39^{0.015}_{-0.014}$	$1.85^{0.02}_{-0.02}$	$2.53^{0.026}_{-0.026}$	$3.53^{0.034}_{-0.034}$	$5.44^{0.042}_{-0.042}$	$9.28^{0.069}_{-0.069}$	$17.1^{0.15}_{-0.15}$	$31.6^{0.47}_{-0.47}$	
$R_s = 341.0^{25.0}_{-24.0}$	M (10^{13} $M_\odot$)	-	0.598±0.007	0.792±0.0083	1.07±0.0098	1.44±0.011	1.93±0.012	2.57±0.012	3.38±0.013	4.68±0.02	7.56±0.062	12.5±0.18	21.6±0.47	
MACSJ0159	r (kpc)	23.4	47.0	77.5	120.4	176.0	259.5	434.9	1311.7					
$\rho_o = 125.0^{100.0}_{-39.0}$	M_g (10^{13} $M_\odot$)	$0.0142^{0.0014}_{-0.0014}$	$0.0596^{0.0034}_{-0.0034}$	$0.15^{0.0086}_{-0.0086}$	$0.339^{0.017}_{-0.017}$	$0.72^{0.027}_{-0.027}$	$1.45^{0.042}_{-0.042}$	$3.47^{0.057}_{-0.058}$	$15.8^{0.27}_{-0.27}$					
$R_s = 700.0^{730.0}_{-270.0}$	M (10^{13} $M_\odot$)	0.17±0.006	0.65±0.022	1.7±0.057	3.7±0.12	7.3±0.25	14.0±0.5	31.0±1.3	130.0±8.0					
MACSJ0242	r (kpc)	24.0	51.2	97.6	208.7	679.0								
$\rho_o = 57.9^{63.0}_{-12.0}$	M_g (10^{12} $M_\odot$)	$0.226^{0.031}_{-0.028}$	$0.974^{0.079}_{-0.14}$	$2.84^{0.21}_{-0.24}$	$9.58^{0.37}_{-0.47}$	$49.7^{1.1}_{-2.6}$								
$R_s = 258.0^{230.0}_{-81.0}$	M (10^{13} $M_\odot$)	0.21±0.022	0.83±0.068	2.5±0.16	7.8±0.7	30.0±5.7								
MACSJ0429	r (kpc)	28.2	58.0	102.8	183.3	336.3	791.1							
$\rho_o = 54.5^{14.0}_{-6.8}$	M_g (10^{13} $M_\odot$)	$0.0202^{0.0028}_{-0.0027}$	$0.0899^{0.0068}_{-0.0066}$	$0.258^{0.019}_{-0.018}$	$0.669^{0.038}_{-0.038}$	$1.75^{0.096}_{-0.096}$	$5.72^{0.34}_{-0.34}$							
$R_s = 202.0^{100.0}_{-51.0}$	M (10^{13} $M_\odot$)	0.32±0.024	1.2±0.064	2.9±0.12	6.7±0.32	14.0±1.1	31.0±4.5							
MACSJ0913	r (kpc)	24.4	45.1	76.1	141.2	336.5	827.3							
$\rho_o = 71.7^{18.0}_{-8.6}$	M_g (10^{13} $M_\odot$)	$0.0159^{0.0015}_{-0.0015}$	$0.068^{0.0039}_{-0.0038}$	$0.184^{0.0071}_{-0.007}$	$0.499^{0.015}_{-0.015}$	$1.69^{0.051}_{-0.051}$	$5.51^{0.27}_{-0.26}$							
$R_s = 305.0^{120.0}_{-57.0}$	M (10^{13} $M_\odot$)	0.23±0.0093	0.71±0.023	1.8±0.046	5.0±0.15	17.0±1.1	46.0±5.0							
MACSJ1423	r (kpc)	31.3	45.8	67.4	99.8	161.4	278.5	618.1	1263.4					
$\rho_o = 70.6^{8.1}_{-6.0}$	M_g (10^{13} $M_\odot$)	$0.0327^{0.0017}_{-0.0017}$	$0.0738^{0.0036}_{-0.0035}$	$0.145^{0.0063}_{-0.0063}$	$0.276^{0.011}_{-0.011}$	$0.604^{0.018}_{-0.018}$	$1.42^{0.038}_{-0.038}$	$4.42^{0.14}_{-0.14}$	$10.7^{0.87}_{-0.84}$					
$R_s = 211.0^{59.0}_{-46.0}$	M (10^{13} $M_\odot$)	-	0.97±0.065	1.9±0.11	3.5±0.16	7.2±0.23	15.0±0.53	33.0±2.3	58.0±5.8					
MACSJ1720	r (kpc)	42.2	90.4	157.8	258.9	450.9	796.6							
$\rho_o = 67.8^{18.0}_{-16.0}$	M_g (10^{13} $M_\odot$)	$0.0462^{0.0029}_{-0.0028}$	$0.176^{0.0091}_{-0.0092}$	$0.504^{0.019}_{-0.019}$	$1.2^{0.041}_{-0.041}$	$2.93^{0.085}_{-0.087}$	$6.48^{0.24}_{-0.24}$							
$R_s = 405.0^{170.0}_{-150.0}$	M (10^{14} $M_\odot$)	0.047±0.003	0.19±0.0094	0.48±0.023	1.0±0.063	2.2±0.2	4.2±0.52							
MACSJ1931	r (kpc)	29.3	36.8	48.2	62.9	77.7	101.3	132.0	174.9	243.7	381.1	917.2	1721.4	
$\rho_o = 126.0^{43.0}_{-22.0}$	M_g (10^{12} $M_\odot$)	$0.299^{0.0096}_{-0.0095}$	$0.522^{0.029}_{-0.027}$	$0.87^{0.048}_{-0.042}$	$1.46^{0.067}_{-0.064}$	$2.14^{0.084}_{-0.079}$	$3.41^{0.1}_{-0.11}$	$5.23^{0.15}_{-0.16}$	$8.2^{0.22}_{-0.23}$	$14.3^{0.31}_{-0.31}$	$28.5^{0.5}_{-0.5}$	$84.1^{2.1}_{-2.1}$	$199.0^{19.0}_{-14.0}$	
$R_s = 851.0^{390.0}_{-200.0}$	M (10^{13} $M_\odot$)	-	0.34±0.0087	0.57±0.014	0.96±0.021	1.4±0.029	2.3±0.042	3.8±0.06	6.3±0.092	11.0±0.19	23.0±0.61	82.0±4.7	170.0±14.0	
MACSJ2046	r (kpc)	59.1	139.0	466.5	957.4									
$\rho_o = 52.9^{16.0}_{-5.3}$	M_g (10^{13} $M_\odot$)	$0.0838^{0.0041}_{-0.0042}$	$0.438^{0.017}_{-0.016}$	$2.55^{0.055}_{-0.087}$	$7.82^{1.1}_{-1.2}$									
$R_s = 210.0^{130.0}_{-45.0}$	M (10^{14} $M_\odot$)	0.11±0.0076	0.44±0.017	1.9±0.26	3.6±0.76									
MACSJ2140	r (kpc)	19.9	33.7	47.5	71.0	101.6	147.4	239.0	523.1	920.7				
$\rho_o = 51.1^{5.2}_{-2.7}$	M_g (10^{12} $M_\odot$)	$0.0837^{0.018}_{-0.018}$	$0.337^{0.027}_{-0.032}$	$0.687^{0.062}_{-0.065}$	$1.52^{0.086}_{-0.12}$	$2.48^{0.33}_{-0.22}$	$4.96^{0.34}_{-0.24}$	$10.4^{0.59}_{-0.63}$	$28.1^{1.3}_{-1.3}$	$57.3^{3.4}_{-3.9}$				
$R_s = 176.0^{36.0}_{-30.0}$	M (10^{13} $M_\odot$)	0.18±0.0075	0.47±0.016	0.85±0.022	1.7±0.031	2.9±0.055	4.9±0.14	9.1±0.45	20.0±1.7	32.0±3.4				
MKW3S	r (kpc)	95.3	103.7	113.8	126.0	140.6	159.5	186.1	223.3	275.3	363.8	567.3		
$\rho_o = 34.9^{12.0}_{-4.3}$	M_g (10^{12} $M_\odot$)	$0.816^{0.011}_{-0.0098}$	$0.966^{0.015}_{-0.018}$	$1.13^{0.025}_{-0.021}$	$1.37^{0.035}_{-0.032}$	$1.68^{0.044}_{-0.043}$	$2.13^{0.05}_{-0.051}$	$2.76^{0.056}_{-0.062}$	$3.65^{0.074}_{-0.078}$	$5.12^{0.095}_{-0.084}$	$7.99^{0.12}_{-0.12}$	$14.1^{0.19}_{-0.19}$		
$R_s = 214.0^{210.0}_{-90.0}$	M (10^{13} $M_\odot$)	-	1.8±0.092	2.1±0.093	2.5±0.091	2.9±0.086	3.5±0.078	4.3±0.077	5.5±0.13	7.1±0.27	9.8±0.58	15.0±1.5		
MS0735	r (kpc)	258.3	271.9	288.2	309.5	339.2	377.8	431.9	513.0	650.9	954.2	1549.8		
$\rho_o = 66.2^{13.0}_{-3.0}$	M_g (10^{13} $M_\odot$)	$0.987^{0.0083}_{-0.0085}$	$1.06^{0.019}_{-0.011}$	$1.16^{0.026}_{-0.02}$	$1.31^{0.029}_{-0.027}$	$1.51^{0.035}_{-0.035}$	$1.76^{0.049}_{-0.048}$	$2.15^{0.063}_{-0.056}$	$2.7^{0.071}_{-0.067}$	$3.8^{0.075}_{-0.072}$	$6.03^{0.11}_{-0.12}$	$11.1^{0.35}_{-0.39}$		
$R_s = 368.0^{27.0}_{-140.0}$	M (10^{14} $M_\odot$)	-	1.1±0.045	1.2±0.046	1.3±0.047	1.5±0.048	1.7±0.048	2.1±0.049	2.5±0.051	3.3±0.069	4.9±0.15	7.4±0.36		
NGC1550	r (kpc)	16.6	20.8	25.9	32.4	40.5	50.7	63.3	79.2	99.0	123.7	154.6	193.3	241.6
$\rho_o = 9.62^{0.25}_{-0.16}$	M_g (10^{11} $M_\odot$)	$0.0891^{0.0023}_{-0.0022}$	$0.13^{0.0052}_{-0.0052}$	$0.202^{0.0086}_{-0.0083}$	$0.308^{0.013}_{-0.013}$	$0.499^{0.016}_{-0.018}$	$0.762^{0.021}_{-0.027}$	$1.17^{0.045}_{-0.04}$	$1.83^{0.082}_{-0.075}$	$2.77^{0.1}_{-0.098}$	$4.15^{0.13}_{-0.13}$	$5.87^{0.26}_{-0.19}$	$7.82^{0.48}_{-0.59}$	$13.4^{0.58}_{-0.73}$
$R_s = 58.7^{5.3}_{-3.7}$	M (10^{12} $M_\odot$)	-	0.84±0.024	1.2±0.028	1.7±0.032	2.4±0.033	3.2±0.029	4.3±0.026	5.7±0.045	7.3±0.094	9.2±0.17	11.0±0.27	14.0±0.41	17.0±0.58
NGC5044	r (kpc)	18.7	23.4	29.2	36.5	45.6	57.1	71.3	89.1	111.4	139.3	174.1	217.7	
$\rho_o = 6.97^{0.2}_{-0.16}$	M_g (10^{11} $M_\odot$)	$0.12^{0.0024}_{-0.0024}$	$0.18^{0.0051}_{-0.005}$	$0.268^{0.0067}_{-0.0078}$	$0.396^{0.01}_{-0.011}$	$0.583^{0.015}_{-0.016}$	$0.806^{0.029}_{-0.029}$	$1.2^{0.049}_{-0.052}$	$1.82^{0.085}_{-0.092}$	$2.78^{0.12}_{-0.12}$	$3.99^{0.2}_{-0.21}$	$5.08^{0.29}_{-0.36}$	$8.99^{0.45}_{-0.45}$	
$R_s = 45.1^{5.4}_{-4.7}$	M (10^{12} $M_\odot$)	-	0.86±0.021	1.2±0.023	1.6±0.022	2.2±0.017	2.9±0.014	3.8±0.034	4.8±0.073	6.0±0.13	7.4±0.2	8.9±0.29	11.0±0.4	
NGC507	r (kpc)	20.1	24.8	30.9	39.5	49.0	62.2	79.4	100.0	126.8	167.0			
$\rho_o = 10.4^{2.4}_{-1.5}$	M_g (10^{11} $M_\odot$)	$0.0713^{0.0095}_{-0.0094}$	$0.109^{0.022}_{-0.022}$	$0.187^{0.031}_{-0.031}$	$0.329^{0.044}_{-0.044}$	$0.55^{0.054}_{-0.054}$	$0.861^{0.072}_{-0.072}$	$1.33^{0.1}_{-0.1}$	$2.1^{0.14}_{-0.13}$	$3.07^{0.23}_{-0.22}$	$6.63^{0.26}_{-0.25}$			
$R_s = 115.0^{77.0}_{-34.0}$	M (10^{12} $M_\odot$)	-	0.77±0.027	1.1±0.033	1.7±0.038	2.4±0.038	3.5±0.042	5.0±0.089	6.9±0.2	9.4±0.39	13.0±0.76			
Perseus	r (kpc)	35.4	44.3	55.4	69.2	86.5	108.1	135.1	168.9	211.1	263.9	329.9		
$\rho_o = 39.3^{0.5}_{-0.46}$	M_g (10^{12} $M_\odot$)	$0.205^{0.00057}_{-0.00056}$	$0.37^{0.0011}_{-0.0011}$	$0.641^{0.0016}_{-0.0016}$	$0.994^{0.0022}_{-0.0022}$	$1.51^{0.0029}_{-0.0029}$	$2.21^{0.0039}_{-0.0039}$	$3.19^{0.0054}_{-0.0054}$	$4.43^{0.0083}_{-0.0083}$	$6.31^{0.013}_{-0.013}$	$8.75^{0.023}_{-0.023}$	$14.4^{0.031}_{-0.031}$		
$R_s = 205.0^{4.9}_{-4.6}$	M (10^{13} $M_\odot$)	-	0.518±0.002	0.763±0.0025	1.11±0.003	1.6±0.0034	2.26±0.0039	3.15±0.0056	4.32±0.01	5.8±0.019	7.66±0.033	9.91±0.053		
PKS0745	r (kpc)	46.5	53.4	61.6	71.5	83.4	97.7	116.3	140.4	176.5	223.6	303.5	495.3	1115.8
$\rho_o = 68.9^{5.3}_{-4.5}$	M_g (10^{12} $M_\odot$)	$0.661^{0.0061}_{-0.006}$	$0.865^{0.011}_{-0.011}$	$1.15^{0.016}_{-0.016}$	$1.53^{0.021}_{-0.021}$	$2.05^{0.026}_{-0.026}$	$2.74^{0.033}_{-0.033}$	$3.77^{0.041}_{-0.041}$	$5.26^{0.051}_{-0.05}$	$7.62^{0.067}_{-0.067}$	$11.3^{0.089}_{-0.089}$	$18.9^{0.12}_{-0.12}$	$35.7^{0.24}_{-0.24}$	$101.0^{1.5}_{-1.5}$
$R_s = 351.0^{50.0}_{-42.0}$	M (10^{13} $M_\odot$)	-	0.83±0.016	1.1±0.02	1.4±0.023	1.8±0.027	2.4±0.03	3.2±0.033	4.4±0.036	6.3±0.051	9.0±0.1	14.0±0.24	26.0±0.78	58.0±3.0
PKS1404	r (kpc)	8.7	13.0	17.8	23.0	29.3	36.8	48.1	64.0	87.7	140.0	260.3		
$\rho_o = 14.4^{0.41}_{-0.37}$	M_g (10^{11} $M_\odot$)	$0.0231^{0.0018}_{-0.0018}$	$0.0599^{0.0039}_{-0.0039}$	$0.134^{0.0065}_{-0.0064}$	$0.241^{0.0095}_{-0.0095}$	$0.396^{0.014}_{-0.014}$	$0.665^{0.019}_{-0.019}$	$1.1^{0.027}_{-0.027}$	$1.85^{0.038}_{-0.038}$	$3.34^{0.057}_{-0.056}$	$7.44^{0.13}_{-0.13}$	$23.6^{0.45}_{-0.43}$		
$R_s = 98.2^{6.0}_{-5.4}$	M (10^{12} $M_\odot$)	-	0.375±0.0062	0.663±0.0097	1.05±0.013	1.59±0.017	2.32±0.02	3.55±0.021	5.44±0.02	8.45±0.042	15.1±0.17	28.8±0.58		
RBS797	r (kpc)	49.0	60.3	76.1	98.1	131.3	194.2	332.7	980.1	1715.1				
$\rho_o = 102.0^{29.0}_{-15.0}$	M_g (10^{13} $M_\odot$)	$0.101^{0.003}_{-0.003}$	$0.148^{0.007}_{-0.0071}$	$0.232^{0.0098}_{-0.0098}$	$0.356^{0.013}_{-0.013}$	$0.592^{0.018}_{-0.018}$	$1.06^{0.027}_{-0.027}$	$2.34^{0.072}_{-0.057}$	$8.72^{0.34}_{-0.33}$	$16.5^{1.9}_{-2.0}$				
$R_s = 421.0^{230.0}_{-110.0}$	M (10^{13} $M_\odot$)	-	1.3±0.056	2.0±0.08	3.2±0.12	5.2±0.18	9.8±0.33	22.0±0.86	77.0±5.7	130.0±12.0				
RXJ1532	r (kpc)	60.1	66.6	74.4	85.4	98.4	115.5	141.0	179.3	244.4	381.2	969.2		
$\rho_o = 93.5^{44.0}_{-17.0}$	M_g (10^{12} $M_\odot$)	$1.34^{0.028}_{-0.028}$	$1.67^{0.037}_{-0.036}$	$2.09^{0.063}_{-0.061}$	$2.64^{0.094}_{-0.093}$	$3.4^{0.12}_{-0.12}$	$4.53^{0.13}_{-0.13}$	$6.21^{0.17}_{-0.16}$	$8.96^{0.22}_{-0.22}$	$14.2^{0.26}_{-0.29}$	$26.2^{0.45}_{-0.34}$	$81.7^{2.4}_{-2.3}$		
$R_s = 502.0^{380.0}_{-150.0}$	M (10^{13} $M_\odot$)	-	1.3±0.048	1.5±0.055	2.0±0.064	2.5±0.073	3.4±0.083	4.8±0.097	7.1±0.14	12.0±0.34	22.0±1.2	70.0±8.9		
Sersic159	r (kpc)	33.1	37.6	43.0	49.5	57.3	67.5	80.7	97.8	125.3	177.4	281.7	552.9	
$\rho_o = 29.6^{2.1}_{-1.8}$	M_g (10^{12} $M_\odot$)	$0.134^{0.0032}_{-0.0032}$	$0.175^{0.0061}_{-0.0056}$	$0.229^{0.0092}_{-0.0084}$	$0.316^{0.012}_{-0.01}$	$0.421^{0.015}_{-0.013}$	$0.574^{0.018}_{-0.018}$	$0.794^{0.025}_{-0.023}$	$1.12^{0.03}_{-0.028}$	$1.7^{0.037}_{-0.035}$	$3.03^{0.055}_{-0.053}$	$5.83^{0.089}_{-0.088}$	$15.1^{0.26}_{-0.25}$	
$R_s = 233.0^{29.0}_{-26.0}$	M (10^{12} $M_\odot$)	-	2.6±0.044	3.4±0.051	4.3±0.058	5.6±0.064	7.4±0.067	9.9±0.065	14.0±0.062	20.0±0.12	33.0±0.44	61.0±1.5	130.0±5.3	

Zw2701	r (kpc)	51.5	59.6	70.1	83.7	101.4	124.5	156.8	201.9	274.2	418.8	1098.2
$\rho_o = 48.8^{6.1}_{-3.5}$	M_g (10^{12} $M_\odot$)	$0.37^{0.022}_{-0.02}$	$0.526^{0.035}_{-0.042}$	$0.747^{0.046}_{-0.05}$	$1.07^{0.05}_{-0.063}$	$1.55^{0.067}_{-0.077}$	$2.2^{0.097}_{-0.11}$	$3.33^{0.13}_{-0.13}$	$5.09^{0.17}_{-0.17}$	$8.23^{0.24}_{-0.24}$	$16.4^{0.3}_{-0.3}$	$55.1^{1.8}_{-1.8}$
$R_s = 248.0^{79.0}_{-49.0}$	M (10^{13} $M_\odot$)	-	0.94±0.039	1.2±0.047	1.7±0.057	2.3±0.069	3.2±0.082	4.5±0.1	6.4±0.15	9.5±0.29	16.0±0.7	38.0±3.1
Zw3146	r (kpc)	10.7	27.2	45.4	63.6	85.4	118.1	170.4	259.4	552.9	2578.5	
$\rho_o = 107.0^{33.0}_{-21.0}$	M_g (10^{12} $M_\odot$)	$0.032^{0.006}_{-0.0056}$	$0.222^{0.024}_{-0.017}$	$0.598^{0.041}_{-0.035}$	$1.29^{0.083}_{-0.051}$	$2.42^{0.1}_{-0.085}$	$4.53^{0.14}_{-0.14}$	$8.43^{0.23}_{-0.24}$	$17.2^{0.33}_{-0.35}$	$49.5^{1.1}_{-0.98}$	$285.0^{9.4}_{-12.0}$	
$R_s = 738.0^{310.0}_{-190.0}$	M (10^{13} $M_\odot$)	-	0.18±0.0048	0.49±0.012	0.94±0.022	1.6±0.036	3.0±0.062	5.7±0.12	12.0±0.28	37.0±1.5	210.0±19.0	